

METASTABLE PHASE EQUILIBRIA IN FACETED/NONFACETED ALLOY
SYSTEMS: AL-GE, FE-B, AND HF-BE

By

THAD MATTHEW ADAMS

A DISSERTATION PRESENTED TO THE GRADUATE SCHOOL
OF THE UNIVERSITY OF FLORIDA IN PARTIAL FULFILLMENT
OF THE REQUIREMENTS FOR THE DEGREE OF
DOCTOR OF PHILOSOPHY

UNIVERSITY OF FLORIDA

1997

Dedicated to my wife, Kimberly, and my daughter, Laurel.

ACKNOWLEDGMENTS

I would first like to thank Dr. Michael J. Kaufman, my advisor, who afforded me the opportunity to undertake this endeavor and who always had an open door to discuss science, politics, life, children, jobs, future, and, most of all, basketball. He was always willing to listen to one of my "what if" scenarios, and no matter how crazy or "out there" it was he never discouraged me from trying it or thinking about it. I would also like to thank my committee members, Dr. Robert Dehoff, Dr. Rajiv Singh, Dr. Reza Abbaschian, and Dr. Wei Shyy, for their patience and willingness to read and advise me during the preparation of this manuscript. I am also deeply indebted to Dr. Neal Evans of Oak Ridge National Laboratory, who supported my work through the SHaRE Research program. I also must thank Dr. Lee Tanner for donating all of his beryllium melt spun ribbon as well as many other materials systems and also Mr. Frank Biancaniello, of NIST, who prepared the iron-boron melt spun ribbons. I would also like to thank Dr. Fritz Grinseng and Mark Emly of Brush-Wellman who helped in performing composition analysis of my Be alloys.

I am deeply indebted to the Microgravity Science and Application Division of NASA who funded this project under grant #NAG8-946.

I would like to thank my peers; without their help and encouragement all of this would have not been possible. Drs. Weaver, Duncan, Costa e Silva, and Jayshankar constantly provided a forum for open discussion on topics of science and such. I would like to thank Dean Paxton and family, who gave encouragement and fun times on the basketball court and with our families; Philip Rack and family, who allowed me to bounce ideas off him and who struggled through this same process simultaneously; Jim Fitz-Gerald, who was always up for a good debate and who was always willing to lend a hand-- I say thank you and God bless. I would be remiss not to thank Ryan Kaufman and Mark Crandall who "worked like champions" as my undergraduate assistants because without their help none of this would have been possible.

Finally, I would like to thank my parents and family who were always there to lend a hand or a checkbook and who constantly encouraged and supported my decision to pursue this degree. My biggest thanks and love go to my wife, Kimberly, who did not know what she bargained for when she agreed to let me stay for this degree and who has constantly supported me and made it possible for me to stay sane when things went wrong; I also must thank my daughter, Laurel, who has been a great joy and the most blessed thing to come into

my life and who will definitely iii make this time always
memorable.

TABLE OF CONTENTS

| | |
|--|-------------|
| ACKNOWLEDGMENTS | iii |
| ABSTRACT | viii |
| 1. INTRODUCTION | 1 |
| 2. BACKGROUND | 4 |
| 2.0 Introduction | 4 |
| 2.1 The Al-Ge System | 4 |
| 2.2 The Hf-Be System | 8 |
| 2.3 The Iron-Boron System | 11 |
| 2.4 Fundamental Thermodynamics and Kinetics | 13 |
| 2.4.1 Thermodynamics of Metastability | 13 |
| 2.4.2 Kinetics--Nucleation | 18 |
| 2.4.3 Kinetics--Growth | 21 |
| 2.4.4 Crystallization Reactions in Metallic Glasses | 24 |
| 3. EXPERIMENTAL PROCEDURES | 38 |
| 3.1 Introduction | 38 |
| 3.1.1 Al-Ge Sample Preparation | 39 |
| 3.2.1 Fe-B Sample Preparation | 41 |
| 3.3.1 Hf-Be Sample Preparation | 42 |
| 4. ALUMINUM-GERMANIUM AND IRON-BORON RESULTS AND DISCUSSION | 46 |
| 4.1 Aluminum-Germanium | 46 |
| 4.1.1 Induction Heated Al-48Ge and Al-52Ge Alloys | 47 |
| 4.1.2 Amorphous Thin Film Crystallization | 48 |
| 4.2 Iron-Boron | 52 |
| 4.2.1 Fe-25B Melt Spun Ribbons | 53 |
| 4.2.2 Fe-27B Melt Spun Ribbons | 54 |
| 4.3 Discussion of Al-Ge and Fe-B Results | 55 |

| | |
|--|------------|
| 5. HAFNIUM-BERYLLIUM RESULTS AND DISCUSSION | 71 |
| 5.1 RESULTS | 71 |
| 5.2 XRD of Bulk Annealed Samples | 71 |
| 5.2.1 X-Ray Diffraction of Hf-45Be Bulk Annealed Samples | 72 |
| 5.2.2 X-ray Diffraction of Hf-50Be Bulk Annealed Samples | 73 |
| 5.2.3 X-Ray Diffraction of Hf-55Be Bulk Annealed Samples | 74 |
| 5.3 TEM of Bulk Annealed Samples | 75 |
| 5.3.1 TEM of Hf-45Be Bulk Annealed Samples | 75 |
| 5.3.2 TEM of Hf-50 Be Bulk Annealed Samples | 76 |
| 5.3.3 Confirmation of Crystal Structures for m-HfBe | 77 |
| 5.3.4 TEM of Bulk Annealed Hf-55Be Samples | 79 |
| 5.4 In-Situ XRD and TEM Studies of Hf-Be Ribbons | 80 |
| 5.4.1 High Temperature XRD of Amorphous Hf-Be Ribbons | 80 |
| 5.4.2 In-situ TEM Hot Stage Microscopy | 82 |
| 5.4.3 Transformation of the m-HfBe Phase | 84 |
| 5.5 Discussion of the XRD and TEM Results | 85 |
| 6. SUMMARY AND FUTURE WORK | 125 |
| 6.1 Summary | 125 |
| 6.2 Future Work | 128 |
| LIST OF REFERENCES | 129 |
| BIOGRAPHICAL SKETCH | 137 |

Abstract of Dissertation Presented to the Graduate School
of the University of Florida in Partial Fulfillment of the
Requirements for the Degree of Doctor of Philosophy

METASTABLE PHASE EQUILIBRIA IN FACETED/NON-FACETED ALLOY
SYSTEMS: AL-GE, FE-B, AND HF-BE

By

Thad Matthew Adams

May, 1997

Chairman: Dr. Michael J. Kaufman

Major Department: Materials Science and Engineering

Determination of whether certain behavior during the microstructural evolution of faceted/nonfaceted alloy systems is general to this class of alloy systems has been carried out. Three different alloys systems (Al-Ge, Fe-B, and Hf-Be) have been examined with respect to the nature of the equilibria between the stable faceted phase and the ordered metastable phase that forms in these respective systems. Many different techniques were used to characterize the evolving microstructures, namely: transmission electron microscopy, scanning electron microscopy, X-ray diffraction, and high temperature X-ray diffraction.

For the Al-Ge alloy system two different processing techniques were employed to study the metastable equilibria. Chill splat samples were prepared via electromagnetic

levitation in a purified Ar environment with the subsequent cooling rate being comparable to wedge mold casting. Thin films were thermally evaporated from previously arc melted buttons. Crystallization of the amorphous films was effected by in-situ heating with the electron beam in a transmission electron microscope.

Fe-B and Hf-Be ribbons were prepared by melt spinning on a copper wheel in an Ar environment. Characterization of these samples was carried out primarily via X-ray diffraction and TEM.

From the microstructural evolution studies of these alloy systems, the stable faceted phase was never directly observed to be in equilibrium with the metastable ordered phase. Thus, for all of these systems a metastable eutectic invariant was proposed between the metastable phase and the stable nonfaceted phase. In addition, a new mechanism involving sluggish/impaired growth of the metastable phase was introduced to explain the phase transformations in samples enriched in the faceting component with respect to the stoichiometry of the metastable phase.

Finally, it is proposed that, in general, system no equilibrium will exist experimentally between the stable faceted phase and the metastable phase for faceted/nonfaceted alloy systems.

CHAPTER 1 INTRODUCTION

A survey of the literature concerning metastable crystalline phase (MCP) formation (and glass formation as well) by Rapid Solidification Processing (RSP) reveals that a common and possibly general characteristic of binary systems where MCP formation occurs readily is the presence of two-phase fields containing at least one equilibrium phase which exhibits faceted growth(1, 2, 3, 4, 5, 6, 7). In fact, it is well documented that faceted growth occurs in materials with anisotropic liquid/solid interfacial energies and relatively high entropies of fusion, ΔS_f , corresponding to a large difference between the entropy of the liquid and solid phases(8). Thus, the formation of MCPs is believed to be related to the slower kinetics associated with the nucleation and growth of the faceted phase(s) and the resulting ability to achieve large departures from equilibrium using non-equilibrium processing methods(9, 10, 11).

While our understanding of the conditions leading to MCP formation has advanced considerably, it is still difficult to produce MCPs in a controlled and reproducible manner. From a theoretical standpoint, it is well established that MCPs, like stable crystalline phases (SCPs), have well-defined thermochemical properties and, therefore, can be treated in a similar fashion. Thus, it is possible to discuss the

similar fashion. Thus, it is possible to discuss the formation of both MCPs and SCPs in terms of their fundamental thermodynamic properties as well as their nucleation and growth kinetics as a function of composition and temperature. Unfortunately, the requisite thermochemical properties of most MCPs remain unmeasured presently due to the difficulty in producing sufficient amounts of them in a controlled manner. This is related to the fact that, in typical systems, there are a number of different, yet competitive reactions that can and do occur simultaneously in order to lower the free energy of the parent phase. These include formation of stable phases, metastable phases, or mixtures of the two, all of which have a lower free energy than the parent phase. Furthermore, the complexity increases even further as solidification/crystallization proceeds since both the composition and temperature of the remaining liquid/glass tend to change as a result of solute partitioning among the growing phases and recalescence due to the release of the latent heat of fusion/crystallization.

In addition, other factors can influence the final transformation product. For example, it is possible for the non-equilibrium structures to decompose to more stable structures during the solidification/crystallization process if there is enough thermal energy and the transformation kinetics are sufficiently rapid. Thus, while it might be possible to form a large volume fraction of a particular MCP

during the initial stages of solidification, it is frequently difficult to produce a single MCP in the bulk of the sample.

Thus, while the subject of metastable phase formation has been the focus of numerous studies, it is by no means well understood how metastable phases nucleate and grow with respect to not only the stable phases in their respective systems but also with respect to other non-equilibrium phases. This subject provides the scope for this work which is as follows: (i) exploration of the metastable phase formation in three faceted/non-faceted systems with emphasis on assessing the relationship between the metastable phase and the stable faceted phase, and (ii) the demonstration of what is believed to be general behavior concerning the equilibrium between metastable phases and stable faceted phases in faceted/non-faceted systems.

Chapter 2 BACKGROUND

2.0 Introduction

Due to the nature of this study, this chapter is be separated into two sections. The first section will deal with a fundamental overview of some of the issues surrounding metastable phase production during RSP with a detailed review of some well-studied RSP systems that laid the foundations for the present work. The last section will provide some theoretical background involving fundamental thermodynamics and kinetics (nucleation and growth) as they pertain to metastable phase formation and their evolution.

2.1 The Al-Ge System

The Al-Ge alloy system (Figure 2.1) has received considerable attention since the early '70s when it was noted that MCP formation was achieved readily in RSP experiments (12, 13, 14, 15, 16, 17, 18, 19, 20, 21, 22, 23, 24, 25, 26). While a large number of different MCPs have been reported, it was shown recently (22) that there are only four distinct MCPs that form in this system, all of which have hypereutectic (Ge-rich) compositions (Table 1). More recently(24, 25), it was shown that the monoclinic (M) and

rhombohedral (R) phases both form metastable eutectics with α -Al implying that metastable equilibria exist between liquid, α -Al and the particular MCP. The hexagonal (H) and orthorhombic (O) MCPs also appear to form metastable equilibria with α -Al only, regardless of whether they form in undercooled liquids or superheated amorphous (or partially amorphous) films(12, 27). In fact, no evidence of metastable equilibria has ever been observed between any two MCPs in this particular system or between an MCP and β -Ge. The latter observations lead to a fundamental question. Specifically, is it possible to have metastable equilibria between an MCP and a stable faceted phase or between two MCPs?

Schematic free energy curves showing the possible equilibria between the hypereutectic metastable monoclinic phase, stable α -Al, β -Ge and liquid (L) phases are shown in Figure 1.2. The diagrams are drawn for three different temperatures: (a) the equilibrium eutectic temperature where the stable α , β and L are all in equilibrium, (b) the metastable eutectic temperature where M is in equilibrium with both α and L, and (c) the metastable peritectic temperature where M is in equilibrium with β and L. In all three schematics, it is clear that M is indeed metastable since there are always two-phase mixtures of α and β with lower free energy. However, it is possible for a supercooled liquid to form a eutectic of α +M in the absence of β , or to combine with β to form M as a metastable peritectic ($L+\beta\rightarrow M$)

in the absence of α (Figure 2.2). Thus, in constructing these thermodynamics based invariants the following assumptions are made: (i) suspend formation of either α -Al or β -Ge, (ii) assume local equilibrium is established, and (iii) the metastable liquidus for either α -Al or β -Ge is constructed by extending the equilibrium liquidus. Since the nucleation and growth (N&G) kinetics of the faceted β phase tend to be sluggish while those of the non-faceted α phase are rapid, then the metastable eutectic ($L \rightarrow \alpha + M$) is achieved readily while the metastable peritectic may be impossible due to the difficulty in suppressing the α phase. Thus, it appears that the observation of metastable equilibrium between the α and M phases, and not between β and M , is explained with these hypothetical constructions and is related to the differences in the N&G kinetics of the various MCPs and SCPs.

Due to the nature of the metastable phase equilibria, it is interesting to consider the formation of MCPs in alloys with compositions enriched in the faceted component (germanium in this case) relative to the stoichiometry of the MCP. For example, it was reported recently (24, 25, 28) that M was observed as the primary phase in hypereutectic alloys containing less than, but approaching ~50 Ge, which was the measured composition of M . However, for compositions above 50 Ge, the microstructures appeared to contain β as the primary phase with either stable ($\alpha + \beta$) or metastable ($\alpha + M$) eutectic in the interdendritic regions. This sudden

transition from primary M to primary β was confusing at first. Closer consideration of the nature of the metastable phase diagram and the schematic free energy curves revealed that, unless the temperature is below that of the metastable peritectic ($L+\beta \rightarrow M$), the M phase will become unstable upon nucleation of β since the common tangent to the $L+\beta$ curves lies below the tangents to both the $L+M$ and $\beta+M$ curves (Figure 2.3). In other words, a mixture of $\beta+L$ has a lower free energy than either the $L+M$ or $\beta+M$ mixtures and, therefore, M should melt upon nucleation of β . Since M formation in germanium-rich liquids will cause the liquid to become enriched in germanium (Figure 3), then it is clear that continued cooling will ultimately result in β nucleation and growth at which point the M becomes unstable with respect to melting.

These observations point out the need for further work in this area. For example, the preceding arguments concerning the "disappearance" of primary M as the germanium concentration was increased above 50% suggest that a primary MCP will always be unstable with respect to melting in alloys enriched in the faceted component. Indeed, it was noted that the R phase in the Al-Ge system behaved in a similar fashion, i.e., for germanium compositions above ~45% (the measured composition of R), the R phase was infrequently observed as a primary phase, whereas in the lower germanium alloys, it was considerably more prevalent(27).

Thus, it appears that this behavior may be general in nature and, therefore, applicable to other systems in which MCPs are common. In fact, there have been essentially no reports of primary MCP formation in compositions enriched in the faceted component and this area is in need of clarification.

2.2 The Hf-Be System

The Hf-Be (Figure 2.4) system has received little attention not only with respect to MCP formation but also with respect to basic equilibrium phase formation(29, 30). This system is faceted/non-faceted in nature if we examine the portion of the equilibrium phase diagram that comprises a eutectic invariant bounded by α -Hf (non-faceted) and HfBe_2 (faceted). This portion of the diagram comprises Be concentrations from 0-67 at% Be. In previous work by Tanner, amorphous and partially crystalline melt spun ribbons of Hf-Be alloys were prepared. These ribbons were then characterized using XRD to determine the starting structure. Tanner, in fact, recognized this weakness in his work as he repeatedly states throughout his article that proper characterization using transmission electron microscopy should be performed. He chooses, however, to draw conclusions based on his XRD data and this is where the results appear contradictory to those in the Al-Ge alloys.

For compositions with up to 5 at% Be, a single phase hcp structure was documented. TEM examinations showed that this hcp phase consisted of acicular martensitic α' formed from primary β on cooling. Microstructures from compositions with increasing Be content were comprised of a combinations of either acicular martensite, pre-dendritic β , metastable m-HfBe or stable HfBe₂. The composition range that could be solidified into a 100% glassy alloy was quite extensive comprising a range of compositions from 30-60 at% Be. Furthermore, Tanner documented the presence of a "metastable ordered phase" (MOP) in both as-solidified and devitrified amorphous ribbons: he determined the structure to be orthorhombic with the Cmcm space group with a stoichiometric composition of 50 at% Be.

In an attempt to determine the mechanisms and reaction paths for the transformation of the glassy ribbons to the crystalline state, differential scanning calorimetry was performed. This work was performed for compositions from the equilibrium eutectic (~42 at% Be) up to 60 at% Be in an argon environment from room temperature to 700 C. As the specimens were heated, they were monitored so that following the appearance of a peak on the calorimeter output, the sample could be quenched and the transformation to that point documented. The main drawback to the overall procedure was that the only subsequent characterization performed was XRD. While XRD is appropriate for determining the majority phases present in the sample, it reveals nothing about the mechanism

of the transformation (i.e., what are the primary, secondary phase(s)) and the microstructural evolution.

Glassy ribbons with between 42 to 45 at% Be were shown by Tanner to undergo a eutectic/eutectoid-like transformation with the resultant product consisting of intermixed α -Hf and m-HfBe. Tanner refers to the spherulitic eutectoid crystallization products seen in Fe-B alloys but one wonders how this type of reaction for his alloys was determined solely with XRD. It was also suggested that the ribbon with 50 at% Be underwent a polymorphic crystallization reaction forming the metastable m-HfBe phase without any compositional change. For ribbons with 55 at% Be Tanner suggests that the following transformation sequence occurs:



From these results, he predicted that m-HfBe forms by a peritectic reaction with $L + \text{HfBe}_2 \rightarrow m\text{-HfBe}$ and he compared this behavior with the Fe-B system where it has been proposed that metastable Fe_3B forms peritectically(31). However, it should be noted that for the Fe-B system, metastable Fe_3B has never been shown to form in alloys with > 25% B the stoichiometric composition for this phase. While it can be shown using schematic free energy curves that these transformation sequences are possible, it would appear that this system is ripe for further investigation and characterization since it appears to contradict the

assertions made based on the Al-Ge system regarding the equilibrium between MCPs and stable faceted phases.

2.3 The Iron-Boron System

The iron-boron system has also received considerable attention over the last 25 years. Numerous studies(31, 32, 33, 34, 35, 36, 37, 38, 39, 40, 41) have been conducted examining the formation of metastable phenomena in this system, and also the subsequent change in magnetic properties with the formation of metastable phases. One of the first investigation into this system with respect to RSP was performed by Koster and Herold who documented the formation of the $Fe_{23}B_6$ metastable phase(31). In addition, they reported that annealing of the metastable Fe_3B phase with an orthorhombic structure for 2 hours at 375 C resulted in the formation of tetragonal Fe_3B . Much of the phase transformations and microstructural evolution work in this system has been performed via devitrification of amorphous melt spun ribbons. Figure 2.5 shows the equilibrium phase diagram for this system. Typically, amorphous ribbons with less than 17 at. %B undergo the transformation sequence illustrated in Figure 2.6, namely, primary α -Fe crystallization which results in boron enrichment of the amorphous matrix and subsequent formation of the metastable Fe_3B phase. For compositions between 17 and 24 at% B, two types of transformations have been documented as shown in Figure 2.7. The first appears to be eutectoid

crystallization ($\alpha \rightarrow \alpha + \beta$) and consists of spherulitic regions containing cores of Fe_3B along with needles of $\alpha\text{-Fe}$. In addition, some researchers have also seen primary crystallization of Fe_3B followed by the formation of secondary $\alpha\text{-Fe}$. Amorphous ribbons of the stoichiometric composition of the metastable Fe_3B phase have been shown to crystallize via a polymorphic crystallization reaction (no compositional change) into the metastable phase (Figure 2.8). It is reported, however, that the composition range for polymorphic crystallization is very narrow (< 1 at%) (34).

From the original work by Koster and Herold, a metastable phase diagram was developed for this system, as shown in Figure 2.9. According to their diagram, the metastable Fe_3B phase forms peritectically. However, close inspection of their proposed diagram raises some interesting issues. First, if the diagram is correct for compositions greater than 25 at% B, there could be a two phase microstructure consisting of Fe_2B and Fe_3B . Several studies, including the one by Koster, no evidence of the metastable Fe_3B phase was found for alloys with greater than 25 at% B regardless of whether the liquid was undercooled or the amorphous phase was "up-quenched". (31, 34, 40). These alloys all displayed primary crystallization of Fe_2B followed by the formation of secondary $\alpha\text{-Fe}$. One such study by Khan et al used Dynamic Temperature X-ray Diffraction (DTXD) to show that for alloys with > 25 at% B, only the two stable phases were produced upon heating amorphous samples from room

temperature to 1300K. However, these authors also proposed another possible phase diagram for this system (Figure 2.10) in which the Fe_3B phase is considered as a stable equilibrium phase above 1420 K. This diagram has met with little acceptance, with most researchers favoring the one by Koster.

With respect to the work by Laoui and Kaufman on Al-Ge alloys, the proposed diagram for the Fe-B system much like that for the Hf-Be system contradicts the assertion that no equilibria exist between the metastable and the stable faceted phases in faceted/non-faceted systems. However, the seemingly analogous results between the observed microstructures for Al-Ge and Fe-B in the literature concerning compositions bracketing the metastable may be significant and was selected for further detailed investigation.

2.4 Fundamental Thermodynamics and Kinetics

2.4.1 Thermodynamics of Metastability

The most common measure of the stability of a changing system is the Gibbs Free Energy, G , which is defined as follows: $G=H-TS$. As the system transforms from one state to the next, this becomes $\Delta G=\Delta H-T\Delta S$ with the Δ 's signifying the change between the two states. According to Gibbs, a system can be considered to be in equilibrium when its energy is at a minimum and will undergo no further change with time. For

the Gibbs free energy function, this condition for equilibrium will be met when $dG=0$ (42). One of the unique features to this condition for equilibrium is that it allows for local energy minima within the system. These states, while not the most stable, are nonetheless states that obey the condition $dG=0$ and are termed metastable equilibria. Since these metastable equilibria have values of G that are greater than the values associated with the absolute minima of the system, these metastable states given time and thermal energy should transform to the stable equilibrium state. For some systems, however, the transformation process from the less stable metastable state to stable equilibrium state can be sluggish such that for all practical purposes the metastable state appears to be the final equilibrium state.

Under conventional solidification conditions (i.e., slow cooling), the phases that form at a given temperature are those predicted by the equilibrium phase diagram. However, under RSP conditions it is sometimes possible to access metastable states within the system producing phases that are metastable in nature and do not appear on the equilibrium phase diagram. An example of this can be seen in Figure 2.11, where A and B are the two stable phases and G is the metastable phase. If we assume that A is the parent phase and that either B or G will nucleate and grow from A, then examination of the driving forces indicates that B has the higher driving force and should nucleate from A. If, for some reason, the formation of B is inhibited, it is evident

that the system can still lower its free energy by activating the metastable state and nucleating G from A. From a thermodynamics viewpoint, this is appropriate since the only criteria for equilibrium according to Gibbs was that of lowest energy (lowest tangent) without any specification of the path to reach that lowest energy state. The construction of metastable equilibria involves common tangent constructions between the stable and/or metastable phase free energy curves that are not the lowest representing equilibrium. Thus, by suspending a stable phase, it is possible to draw metastable phase fields and their relation to the non-suspended phases on the diagram. Examples include the Fe-Fe₃C and Al-m-AlGe metastable diagrams.

It should be mentioned that, due to the large deviations in the solute partitioning that are frequently associated with RSP, some researchers prefer metastable equilibria constructions that are not simple extensions of the equilibrium phase boundaries; i.e., these constructions are not based on fundamental thermodynamics but rather kinetics (nucleation and growth) factors for the determination of the metastable "phase boundaries." The manifestation of these kinetic factors is most easily monitored by examining the change in the partition coefficient, $k (=C_s/C_L)$ with processing conditions. As solidification velocity is increased, the partition coefficient may deviate from its equilibrium value, k_e , towards unity, which represents complete solute trapping (Figure 2.12). This phenomenon is also explained by

examining the interface velocity of the growing solid (v); for the case where $v \ll v_p$, there is sufficient time for solute redistribution; as v continues to increase to the point where $v \gg v_p$ then the liquid composition is incorporated into the solid as the interface advances. Kinetic interface condition diagrams (Figure 2.13) as developed by Aziz (103) are used to depict the changes of the liquidus and solidus curves based on the aforementioned kinetic conditions. These kinetic interface condition diagrams can serve as guidelines for the bounds of the metastable equilibria as determined thermodynamically.

Another example of the activation of a metastable state achieved by RSP is that of amorphous or metallic glass formation. Cohen and Turnbull predicted that if crystallization could be avoided, all liquids would form glasses(43, 44). The two main classes of metallic glass formers are as follows: (i) transition metal-metalloid systems, where the metalloids include B, C, P, Si, Ge, and (ii) transition metal-transition metal systems, such as Cu-Zr, Cu-Ti and Ni-Nb(45, 46). Over the years, many different criteria have been used to try to predict glass formation and glass forming tendency (GFT). From Duwez and co-workers original success of forming a metallic glass in Au-Si alloys, the initial quality of systems with a high GFT was thought to be the presence of a "deep eutectic."(3, 47) This concept was later modified by Massalski(48) who proposed that the concept of "deep eutectics" should be changed to "plunging To

curves." The T_o curves are the curves that represent the locus of points at which the free energy of the solid and liquid are equal. For the case where the glass transition temperature (T_g) lies below the T_o curves, if a liquid is undercooled below the T_o curves, crystallization is expected to occur since no solute partitioning/redistribution is necessary. In order to avoid crystallization and thus form a metallic glass, it would be more appropriate if T_g lies above the T_o curves, thereby allowing T_g to be reached before the T_o curves during undercooling.

In addition, there have also been several semi-empirical attempts at using basic thermodynamic information provided from the phase diagrams for alloy systems to predict GFT. Sapean and Turnbull(46, 49) both proposed that from the literature it can be shown that for values of the reduced glass transition temperature (T_{rg}) > 0.45 , easy glass formation is expected. The value for T_{rg} is defined as T_g/T_l , where T_l is the liquidus temperature for the alloy. Marcus and Turnbull(50), in an attempt to refine the prediction of GFT, developed a more complex criterion for ease of glass formation based on the magnitude of the negative deviation of the actual liquid ideal solution behavior. Specifically, as the negative deviation from ideality increases, so does the GFT. This correlation was somewhat successful at predicting GFT; although, it failed to predict the behavior of certain phosphorous-containing alloys; this was attributed to the volatility of phosphorous. Lastly,

Donald and Davies(51) used a simplified rule of mixtures approach and showed that for $T^* > .2$ a glass could be formed for cooling rates of the order of 10^6 K/sec. The value of T^* relates the deviation of the actual system liquidus from that predicted by a simple rule of mixtures.

2.4.2 Kinetics--Nucleation

While thermodynamics is quite valuable for determining what reaction paths are possible, the reaction sequence(s) that occurs also depends on the kinetics of both nucleation and growth. The first topic for discussion concerns the nucleation of phases and since the bulk of this research is centered on the transformation in metallic glasses, nucleation will be discussed from the viewpoint of crystallization or devitrification of a metallic glass.

The steady-state homogeneous nucleation frequency equation resulting from that of Becker and Doring can be written as follows(52, 53, 54, 55):

$$I_s = A/\eta \exp[-16\pi\sigma^3/3k_B T \Delta G_v^2] \quad (2.1)$$

where I_s = nucleation rate in $(m^{-3}s^{-1})$

ΔG_v = free energy for crystallization (J/m^3)

σ = solid/glass interfacial energy (J/m^2)

η = glass/liquid viscosity $(Pa s)$

k_B = Boltzman's constant

T = Absolute Temperature (K)

For heterogeneous nucleation where nucleating agents/catalysts are present, it is necessary to include a

contact angle term, $f(\phi) = (2+\cos\phi) (1-\cos\phi)/4$ where ϕ is the contact or spreading angle at the solid-glass interface(56). This term is included in the exponential term of the nucleation rate equation and accounts for the reduced surface area of the nuclei resulting during heterogeneous nucleation.

From equation 2.1, it is evident that the three main material parameters that exhibit the greatest influence on nucleation are η , σ , and ΔG_v in equation 2.1. With increasing undercooling the viscosity of a liquid increases by several orders of magnitude as shown in Figure 2.14. This behavior is defined by the Vogel-Fulcher(57, 58, 59) equation as follows:

$$\eta = B \exp[b / (T - T_b)] \quad (2.2)$$

where B and b are constants and T_b is the temperature below the glass transition temperature. Thus, we can see that for nucleation events occurring around T_g the viscosity of the glass/liquid can play a substantial role. The solid/glass (liquid) interfacial energy and the free energy for crystallization ΔG_v , however, possess the greatest influence on the nucleation rate since they are raised to the powers of 3 and 2, respectively, within the exponential. It is quite ironic that the two parameters that exhibit such a strong influence on the nucleation rate are also the most difficult to determine experimentally. There have been numerous studies, for instance, trying to determine the value for

solid/liquid interfacial energy that have met with limited success due to experimental problems such as surface oxidation of the solid or liquid(60, 61). There have been several attempts(49, 62, 63, 64) at developing formulation to determine σ two of the more successful approximations for σ have been given by Uhlman and Turnbull,(55, 65) with Uhlmans' approximation for the molar interfacial free enthalpy given as

$$\sigma_m = K' \sigma V^{2/3} N^{1/3} \quad (2.3)$$

where N is Avogadros number and V is the molar volume, and K' , a constant that is related to the interfacial packing. Turnbull's expression for σ_m involves the volume melting enthalpy and a constant a that he determined to be ~ 0.45 for most metallic systems. The combination of these two expression leads to a plausible expression for the solid/liquid interfacial energy term which is as follows:

$$\sigma = a / K' \Delta H_f^f V (V^{1/3} / N) \quad (2.4)$$

The most basic of the approximations for the driving free energy of crystallization was given by Hoffman(66) as

$$\Delta G_V = T_r \Delta T_r \Delta H_f^f V \quad (2.5)$$

where T_r is the reduced temperature T/T_m , ΔT_r is the reduced undercooling= $(T_m - T)/T_m$ and $\Delta H_f^f V$ is the volume enthalpy of

melting. It should be noted that this expression will hold true only if the heat capacities of both the glass (liquid) and solid are equal and independent of temperature. There have been numerous other attempts at developing expression for ΔG_v and one of the more common when discussing metallic glasses is that by Thompson and Spapean(67) as follows:

$$\Delta G_v = 2\Delta T_r [T_r / (1+T_r)] \Delta H_f^f v \quad (2.6)$$

where

T_r = Reduced melting temperature = T/T_m

ΔT_r = Reduced undercooling = $(T_m - T)/T_m$

$\Delta H_f^f v$ = Enthalpy of fusion/unit volume

which according to Thompson and Spapean can be approximated as $\Delta H_f^f v = N_0 K \beta T_m / V$ (55).

2.4.3 Kinetics--Growth

As important as the nucleation stage is to the phase selection process, the crystal growth stage can play just as large a role as controlling the final microstructure.

Figure 2.15 shows a plot developed by Perepezko (68, 69) to demonstrate the influence of growth rate on the resulting microstructure following RSP. Considering crystal growth in metallic glass systems, viscosity plays a more dominant role than in conventional solidification(68, 69, 70, 71, 72). A common expression for crystal growth in glassy systems developed by Turnbull(65, 73, 74) is as follows:

$$u_C = f D_g / a_0 [1 - \exp(-\Delta T_r \Delta H_m^f / RT)] \quad (2.7)$$

where D_g is the diffusion coefficient at the solid/glass (liquid) interface and f is the fraction of sites available for growth at the interface. For the situation where the interface is rough corresponding to phases with low entropies of fusion, all sites are considered to be equal and $f=1$. In the case of faceted growth, defined by phases with high entropies of fusion, all of the interfacial sites are not equal for growth and $f=0.2 \Delta T_r$. The value for D_g is taken from the bulk liquid diffusivity, D , which can be related to viscosity of the glass/liquid through the Stokes-Einstein equation with $D=kT/3\pi a_0 \eta$. Recently however, work by Greer(59) has shown that for the case of crystallization below T_g , there are significant stress effects that lead to a breakdown of the Stokes-Einstein relationship for amorphous alloys. In spite of this complication there has yet to be proposed another relationship between viscosity and diffusivity that can be applied in quantitative treatments, and, therefore, the Stokes-Einstein relationship must still be used with its flaws duly noted. It is important to note that for crystallization that relies on compositional redistribution, as is often the case in alloy crystallization, the diffusion coefficient at the interface can in fact be the limiting factor to growth and to the final distribution of phases in the microstructure(45, 70, 71, 72). From Figure 2.16, which shows the crystal growth rate plotted

versus undercooling, we see that at relatively low undercoolings the growth rate is high but that as the level of undercooling increases the growth rate continues to decrease even up to T_g . Thus, during the crystallization/devitrification of an amorphous solid the growth rate around T_g is relatively slow; this, coupled with a relatively large driving force for nucleation in this temperature regime, leads to the very refined nanoscale microstructures that have received much attention in the last 5 years.

Another expression for the temperature dependence of crystal growth developed by Rawson and Fine(75, 76) is as follows:

$$u = u_0 \exp(-Q_g/RT) [1 - \exp(-\Delta G/RT)] \quad (2.8)$$

where u_0 = pre-exponential factor $\sim 10^3$ m/s
 Q_g = activation energy for atomic transport across the amorphous-solid interface
 ΔG = Free energy/mole of crystallization

For the situation where the system is highly undercooled as is the case with metallic glasses, $\Delta G \gg RT$ and thus the second term in equation (2.8) vanishes leaving the growth rate for the crystallization of a metallic glass to obey an Arrhenius type relationship.

A natural outcome of the preceding discussion of nucleation and growth as it pertains to metallic glass is the concept of critical cooling rate, R_c , to avoid nucleation. The critical cooling rate is the necessary cooling rate so that an alloy on undercooling will miss the knee of a CCT curve and thus form a metallic glass. There have been several investigators who have attempted to develop an expression for R_c (77, 78, 79, 80). In 1969, Turnbull(81) predicted that a cooling rate of 10^6 K/s was necessary for glass formation based on simple nucleation theory in which he stated that the melt viscosity and the magnitude of the parameter $(\alpha\beta^{1/3})$ in which α and β are functions of interfacial energy, ΔH_f , ΔS_f , and atomic volume control the ability of the system to avoid nucleation. The most successful prediction was that by Uhlmann(65, 82), who developed a treatment based on Johnson-Mehl-Avrami-Komologrov (JMAK) transformation kinetics to predict that the necessary cooling rate to produce amorphous elemental silver and nickel was approximately 10^{10} K/s. The final form of Uhlmann's equation for critical cooling rate was $R_c = \Delta T_n/t_n$ where ΔT_n is the amount of undercooling and t_n is the minimum time for crystallization.

2.4.4 Crystallization Reactions in Metallic Glasses

As a result of the amorphous or glassy phase being metastable in nature, it should undergo a transformation event upon heating when the kinetics of atomic motion become

sufficiently fast. During heating, amorphous solids have been shown to go through one of the following three transformations sequences as shown in Figure 2.17(31).

Primary crystallization involves the formation (N&G) of a crystalline phase of a different composition in an amorphous matrix, be it a stable phase or intermediate metastable phase. For a binary alloy, as this reaction occurs, the amorphous matrix becomes enriched in one of the components depending on the stoichiometry of the primary phase. This enrichment will continue until the composition in the amorphous matrix reaches either a stable or metastable phase boundary and thus transforms accordingly.

Polymorphic crystallization can be thought of as partitionless solidification in that the parent and product phase have the same composition. During polymorphic crystallization, the amorphous solid transforms into either a supersaturated solid solution phase, a stable compound or an intermediate metastable compound without any change in composition (Figure 2.17). This reaction most commonly occurs when the overall composition of the amorphous solid is at or near the composition of the phase to which it transforms.

Eutectoid crystallization is somewhat similar to what we know as a eutectoid decomposition in solids. In this case, two phase crystallize simultaneously: these two phase may be either the two stable equilibrium phases or a combination of stable and metastable phases. It is noted however, that

although the two phases form simultaneously, the reaction in many cases does not involve coupled growth as is frequently the case in both eutectic solidification from a liquid or eutectoid decomposition in a solid. Since this reaction requires redistribution of the component atoms, it often has slower kinetics than the polymorphic or primary crystallization reactions.

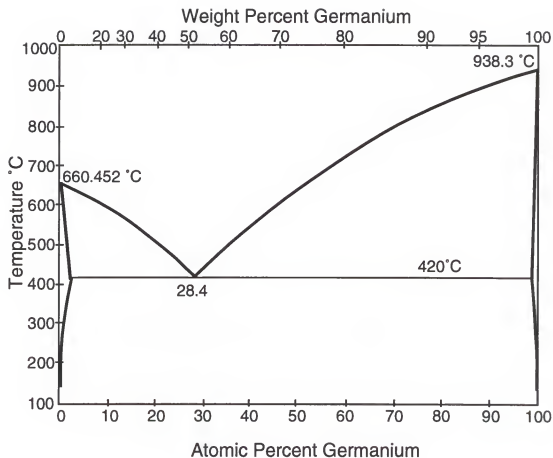


Figure 2.1. Al-Ge equilibrium phase diagram (26).

Table 2.1. Metastable phases in the Al-Ge alloy system (22).

| Metastable Phase | Space Group | Lattice Constants | Composition (at. %) |
|------------------|--------------------|--|---------------------|
| Monoclinic | P2 ₁ /c | a=0.673, b=0.582, c = 0.805 nm b=147.85° | ~50%Ge |
| Rhombohedral | R3c | a=0.767 nm, a=94.54° | ~45%Ge |
| Orthorhombic | Pbca | a~0.78, b~0.57, c~0.73 nm | 41-50%Ge |
| Hexagonal | P6/mmm | a~1.40, c~0.72 nm | 42-45%Ge |

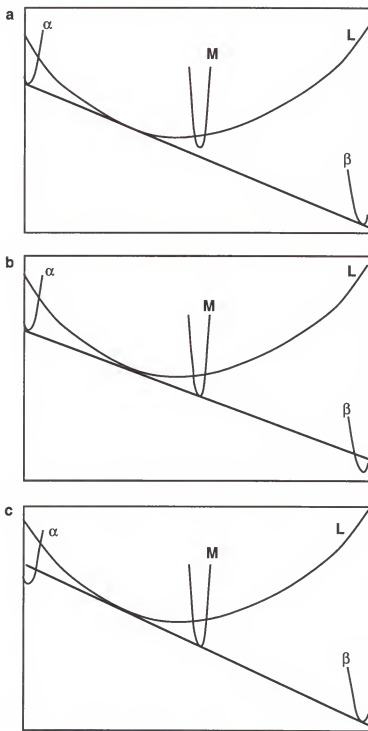


Figure 2.2. Schematic of Free energy curves: (a) equilibrium eutectic ($L \rightarrow a\text{-Al} + b\text{-Ge}$) (b) metastable eutectic ($L \rightarrow a\text{-Al} + M$) (c) metastable peritectic ($L + b\text{-Ge} \rightarrow M$).

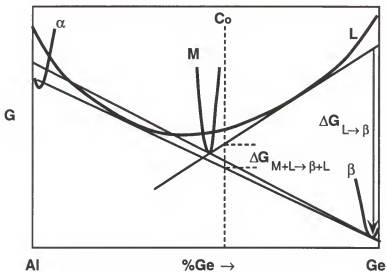


Figure 2.3. Schematic free energy curves illustrating the lower free energy of the $L+\beta$ mixture compared with both $L+M$ and $\beta+M$ mixtures (26).

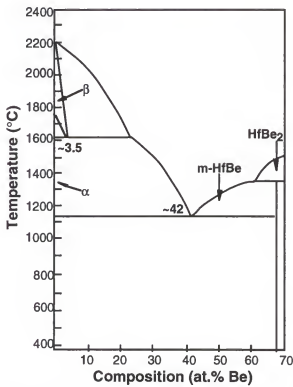


Figure 2.4. Hf-Be equilibrium phase diagrams (30).

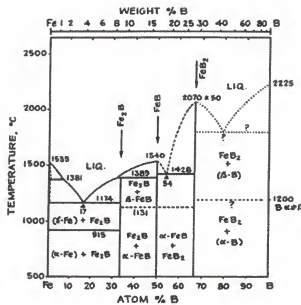


Figure 2.5. Fe-B equilibrium phase diagram (31).

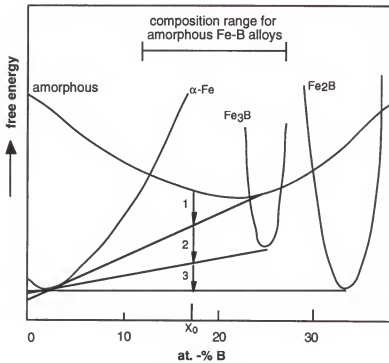
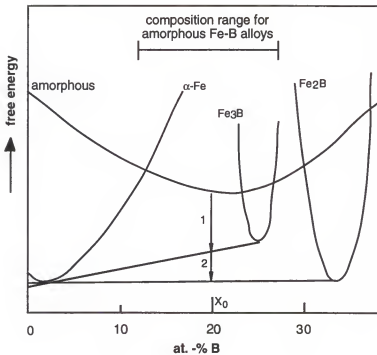
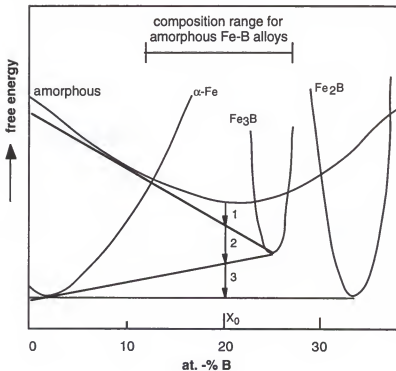


Figure 2.6. Schematic Free Energy Curves depicting the crystallization of amorphous Fe-17B alloy.



(a)



(b)

Figure 2.7. Schematic Free energy curves depicting the two different crystallization reactions documented for Fe-B_x alloys with 17x24.

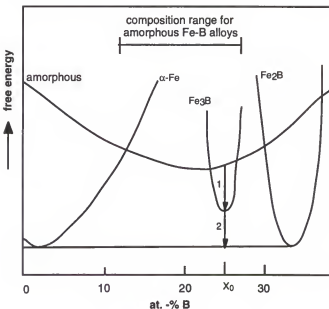


Figure 2.8. Schematic Free energy curves depicting the polymorphic crystallization in Fe-25B alloys.

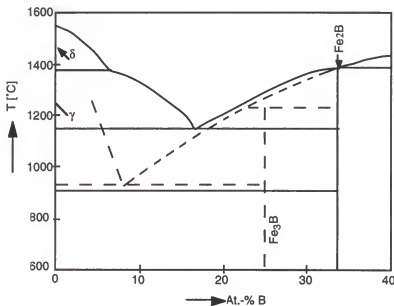


Figure 2.9. Fe-B metastable phase diagram as proposed by Koster and Herold (31).

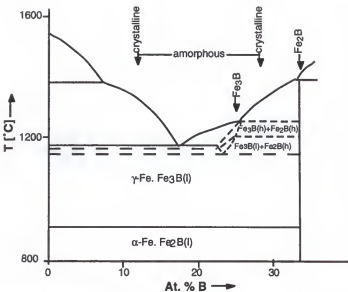


Figure 2.10. Fe-B equilibrium phase diagram as proposed by Sostarich et al (34).

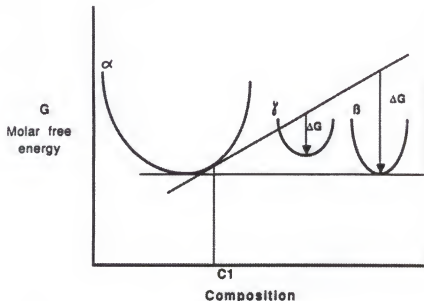


Figure 2.11. Schematic Free energy curves showing the influence of nucleation on the resulting microstructure.

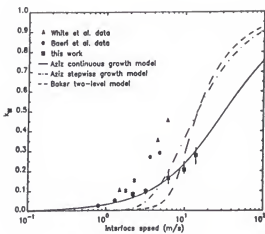


Figure 2.12. Dependence of partition coefficient on interface velocity--triangles and circles velocity estimated from heat flow calculations, squares velocity measured by transient conductance (103).

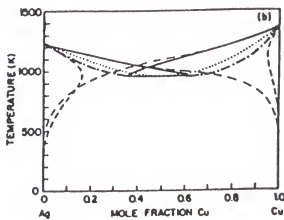


Figure 2.13. Kinetic interface condition diagrams for Ag-Cu for an imposed interface speed of $10v_b$ (103).

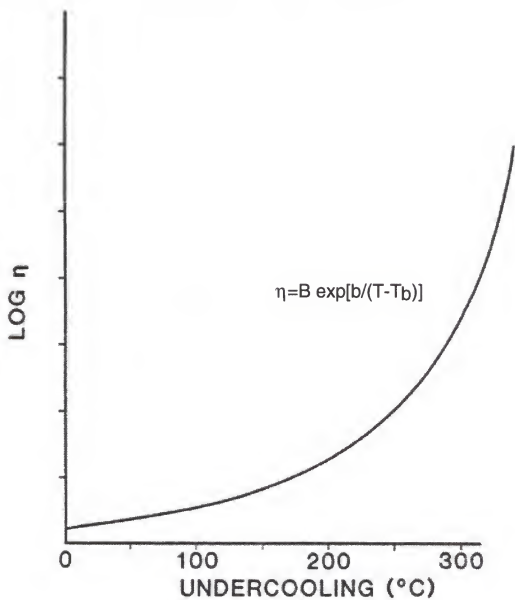


Figure 2.14. Schematic Plot of Vogel-Fulcher equation depicting the relationship between viscosity vs. undercooling.

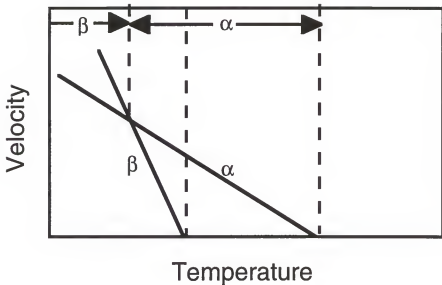


Figure 2.15. Schematic plot of growth velocity vs. temperature showing the effect of crystal growth rate on the final microstructure (65).

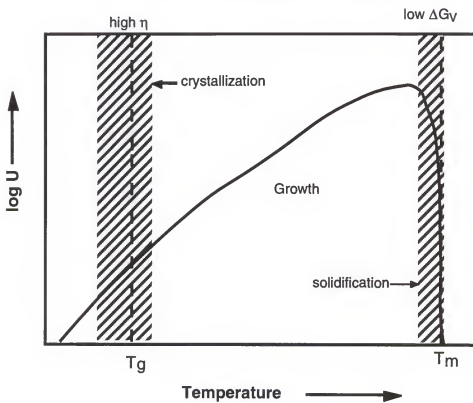


Figure 2.16. Schematic plot of crystal growth rate vs. undercooling.

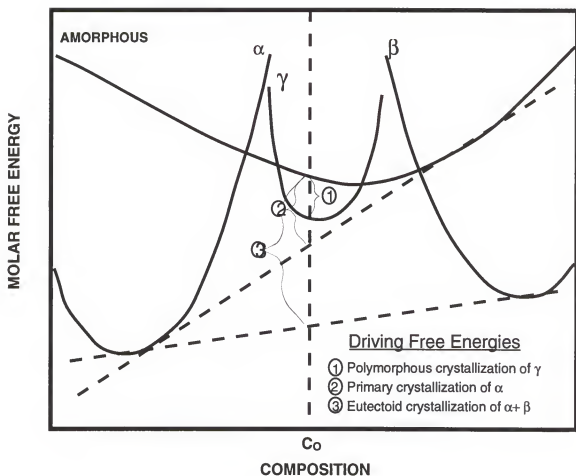


Figure 2.17. Schematic of free energy curves representing the possible transformation reactions during crystallization (31).

CHAPTER 3
EXPERIMENTAL PROCEDURES

3.1 Introduction

Three different alloy systems were investigated during the course of this study. Al-48.52Ge alloy buttons were prepared from their respective high purity elements via non-consumable arc melting under a purified Argon environment. The Al-55Ge thin film used in this study was prepared via thermal evaporation from a previously arc melted button.

Fe-25.27B alloy buttons were produced from high purity elements also via arc melting in a purified Argon environment. Ingot sections were then used to make melt spun ribbons. Melt spun ribbon samples were produced both at UF and also at NIST by Frank Biancaniello.

Hf-45.50, and 55Be, alloy ingots were prepared from high purity elements via arc melting in an Ar environment. Compositions that showed high volume fraction of the glassy phase during arc-splat/hammer-and-anvil sample were then used for melt spinning.

The remaining portions of this chapter will be subdivided into sections describing the detailed procedures used to prepare and characterize these materials.

3.1.1 Al-Ge Sample Preparation

Arc melted buttons with total weight of approximately 1 to 1.5 grams were used to produce chill splats via induction heating and levitation using the electromagnetic levitation (EM) processing facilities at the University of Florida. Figure 3.1 shows a schematic of the EM facilities which consist of a Lepel high frequency generator, a step down transformer, an induction/levitation coil, and a copper chill plate.

The Al-Ge buttons were heated/levitated to approximately 700° C in an Ar-He environment followed by turning off the power and allowing the specimens to drop onto a copper chill plate. The chill splats produced with this technique are estimated to have experienced cooling rates slower than melt spinning (10⁵ K/s) but faster than wedge mold chill casting (\approx 100 K/s).

Once the chill splats were produced initial characterization using XRD was performed to verify the production of metastable phases. Following XRD samples were mounted in Buehler cold-mounting epoxy and prepared for optical microscopy. Initial polishing was performed using 240-1200 grit SiC wet grinding papers followed by final polishing using 1.0.3, and 0.05 μ m Al₂O₃ polishing solution on a Leco Lecloth polishing cloth. The samples were then etched with a solution consisting of 5ml H₂O, 25ml HF, and 25ml HNO₃.

The microstructures of the etched samples were then examined by optical microscopy, using a Nikon NEOPHOT 21 optical microscope and also by SEM in a JEOL 35CF scanning electron microscope in the back-scattered electron image mode.

The Al-55Ge thin films were deposited onto single crystal NaCl substrates and floated off onto 3mm Cu grids by immersing in de-ionized water. These films were produced by Dr. Michael Kaufman during his work on his Ph. D. dissertation at the University of Illinois-Urbana.

Determination of the composition of the film was performed using film was produced via thermal evaporation form an Al-80Ge button. The button was doped heavier with Ge than desired for the film since only a single source thermal evaporation unit was available and since Al-will begin to evaporate at a lower temperature and at a faster rate than Ge. The film was deposited a JEOL 4000FX transmission electron microscope equipped with a PGT EDS detector. The technique used to determine film composition is that developed by Cliff and Lorimer and will be described in greater detail in the following chapter.

In-situ heating of the film to effect crystallization was performed using the electron beam in a JEOL 200CX TEM operating at an accelerating voltage of 200 KV. By focusing the electron beam onto the appropriate area of the sample and then removing the smallest condenser aperture and inserting the largest condenser aperture the electron beam can act as a

local heat source. Cooling was effected by re-inserting the smallest condenser aperture while simultaneously defocusing the incident electron beam. Using this technique the film was heated to a temperature where it would crystallize but below that where melting would be expected.

3.2.1 Fe-B Sample Preparation

Melt spun ribbons of the alloys of interest were produced both at the University of Florida and at NIST using a conventional melt spinning device. The alloys were induction melted in quartz tubes coated with ZrO_2 ceramic mold wash to prevent any reaction between the molten alloy and the tube and forced through a small opening at the end of the tube using purified Ar gas pressure, onto a copper wheel rotating at approximately 25 m/s (UF) and 4000-6000 rpm (NIST). All of the ribbons were produced under a purified Ar environment following several evacuations (50 mtorr) and backfills (Ar) before spinning. None of the ribbons produced were amorphous as hoped resulting most likely due to the high viscosity of the melt in this composition range which made rapid proper ejection from the tube difficult.

Initially, all of the samples were characterized by XRD using a Phillips 3720 Diffractometer. Thin foils from the Fe-25B and Fe-27B sample batches were then prepared by sectioning and grinding 3mm sections using 800 and 1200 grit SiC to create smooth parallel surfaces; these were then pre-thinned electrolytically, followed by argon ion thinning

using a Gatan Dual Ion Mill. Microstructural characterization was performed in a JEOL 200CX TEM.

3.3.1 Hf-Be Sample Preparation

Hf-Be melt spun ribbons containing from 45-55 at%Be were obtained from Dr. Lee Tanner formerly of Lawrence Livermore Laboratories. These alloys were produced from high purity materials by arc melting under purified argon. Those compositions that produced high volume fractions of the glassy phase during splat quenching were subsequently melt spun into ribbons of 10-30 microns thickness and 1-2 mm width.

Initial characterization was performed on the ribbons in the as-spun condition using a Phillips 3720 X-ray diffractometer. Both the wheel and air side of the ribbons were x-rayed with no apparent differences being discernible.

Bulk furnace annealing of ribbons with 45-55 at% Be was performed using ribbon samples that were encapsulated in quartz tubes with an inert, purified argon backfill along with Ta gettering strips. The encapsulated samples were then annealed in a single zone tube furnace at 500-525 C for times ranging from 5-65 minutes. The temperature was monitored via a Type K thermocouple placed next to the quartz ampoule during heating. After their prescribed annealing treatment, the quartz ampoules were quenched in water. Visual examination of the ribbon surfaces and the Ta gettering strips was made to assess the level of oxidation

during annealing. Any samples that showed any signs of surface discoloration were discarded and re-run.

Characterization of the annealed ribbons involved both XRD and TEM using the JEOL 200CX microscope. Thinning of the specimens for TEM was performed using two methods as follows: (i) electropolishing to perforation using Spurling's solution (5% H₂SO₄ in methanol) at -50 C and 12 V, (ii) electro-dimpling using 90% acetic-10% perchloric (PACE) followed by ion milling. The latter method produced more acceptable foils and by the end of the work was used almost exclusively.

High temperature XRD was performed in a Philips high temperature X-ray diffractometer. Amorphous ribbon samples were attached to a Ta heating strip using graphite paint. The temperature of the strip and sample was monitored via a thermocouple attached to the underside of the Ta heating strip just below the position of the sample. Oxidation of the samples was controlled by using a He gas purging system that kept a steady flow of He through the specimen chamber at all times. The heating schemes for the ribbon samples were devised to mimic as close as possible the DSC/DTA ramp rates and thus sample were heated to 470 C at 20C/min followed by XRD sampling every 10 C up to 640 C. It should be noted that the XRD scans took approximately 5 minutes to run thus creating some lag time between temperatures.

In-situ heating in the TEM was also performed both at UF using a Gatan hot straining stage holder in a JEOL 4000FX microscope and at Oak Ridge National Laboratory under the

SHaRE program using a Gatan hot stage holder in a Phillips CM12 microscope. Amorphous samples were heated to between 500 and 600° C and the resulting phases and microstructural evolution was characterized using bright field microscopy (BF), selected area diffraction (SAD), and convergent beam electron diffraction (CBED).

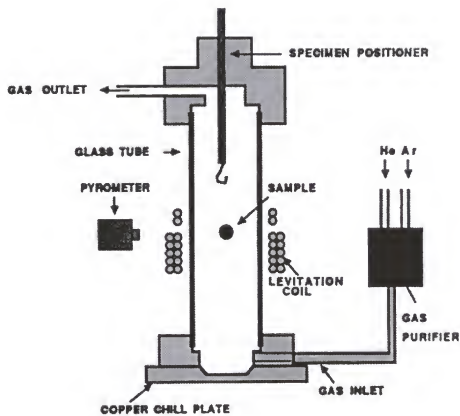


Figure 3.1. Schematic of EM Levitation Unit (9).

CHAPTER 4
ALUMINUM-GERMANIUM AND IRON-BORON RESULTS AND DISCUSSION

4.1 Aluminum-Germanium

Throughout the past 25 years the Aluminum-Germanium system has received much attention with respect to metastable phase formation. Previous work on this system by both Kaufman and Fraser and Laoui and Kaufman lead to the present investigation concerning the phase equilibria in faceted/non-faceted systems. As a result, it was deemed necessary to perform some confirmation experiments to reproduce the previous work on Al-Ge as a starting point for this work. To date, the phase equilibria in this system have been investigated using many different RSP techniques including: melt spinning, atomization, wedge mold chill casting, splat quenching, and amorphous thin film deposition and subsequent crystallization. The technique employed for our initial studies of this system was that of induction heating in an electromagnetic levitation system, which eliminates contamination from crucible wall interactions, followed by dropping the levitated sample onto a copper chill block. This technique produced samples that were cooled at rates estimated to be slower than those characteristic of melt spinning. Following these initial experiments, the focus

turned to an amorphous Al-Ge thin film produced by thermal evaporation. The approximate composition of the film had to be determined using quantitative EDS analysis. The desired composition was approximately 55 at% Ge for the film since a survey of the literature showed little if any reported data for amorphous thin films greater than 50 at% Ge. It was decided that examination of the transformations in an amorphous film would be interesting to compare to the results obtained for samples quenched from the liquid that were enriched in Ge with respect to the stoichiometric composition of the metastable phases that form.

4.1.1 Induction Heated Al-48Ge and Al-52Ge Alloys

Examination of an Al-48Ge specimen levitated and induction heated to approximately 750 C and dropped on a copper chill block shows large amounts of primary metastable monoclinic phase with some β -Ge particles present and either stable or metastable interdendritic eutectic present (Figure 4.1). XRD data from the 48Ge samples also confirm the presence of the monoclinic phase.

The Al-52Ge chill splat sample was processed under the same conditions as the Al-48Ge alloy. It is interesting to note that, instead of a large amount of primary monoclinic phase, the primary phase in this alloy is the β -Ge phase (Figure 4.2).

These results support the original results by Laoui and Kaufman on this system and their explanation of the re-

melting of the primary monoclinic phase for a sample with 52 at% Ge. Figure 4.3 displays a plot of the free energy versus composition diagram for this system. For the Al-48Ge sample, the transformation can be attributed to the reaction path demonstrated by Sequence I. For the Al-52Ge alloy, a more complex, transformation scheme is devised which has the primary monoclinic phase nucleating from the liquid (step 1) followed by the subsequent Ge enrichment of the liquid which provides a rather large driving force for β nucleation. It can be shown that a mixture of $M+\beta$ will lower the system free energy but that further inspection shows that a mixture of $L+\beta$ could lower the free energy even more (Figure 4.4). Thus, as proposed by Laoui and Kaufman re-melting of the monoclinic phase would provide the $L+\beta$ mixture necessary and would account for the lack of any primary monoclinic phase in the final microstructure.

4.1.2 Amorphous Thin Film Crystallization

Crystallization of an amorphous thin film via in-situ heating with the electron beam in the TEM was performed. The film was prepared via thermal evaporation of the two elements and as a result it was necessary to perform compositional analysis to determine the starting composition of the film. Compositional analysis of thin film samples can be performed by using quantitative EDS. The most common method used to generate relative compositions of the species present is to relate the integrated peak intensities for the characteristic

peaks to the relative concentrations. The method for making this comparison was developed by Cliff and Lorimer (83) and the relationship is as follows:

$$C_a/C_b = K_{ab} I_a/I_b \quad (4.1)$$

where C_a and C_b are the concentrations of the two elements in the alloy and I_a and I_b are the integrated intensities of the characteristic peaks for each element. The value for K_{ab} is referred to as the Cliff-Lorimer factor which takes into account the fluorescent yield, fraction of the total intensity measured, atomic weight, and the ionization cross-section for each element(84). In some cases the Cliff-Lorimer factor has already been tabulated but if it is not, one method for generating this value is to use a phase with a known composition composed of the same elements as the sample in question and then back calculate from equation (3.1). This is precisely the method used in our compositional analysis. An Al-36Ge melt spun ribbon sample containing the monoclinic metastable phase with a 50-50 composition was used. Figure 4.5 displays an EDS spectrum collected from this phase. From the integrated peak intensities for the Al- $K\alpha$ and Ge- $K\alpha$ peaks, a Cliff-Lorimer factor, K_{GeAl} , was determined to be approximately 0.549. The corresponding composition of the film was determined from the EDS spectrum in Figure 4.6 and was calculated to be approximately, 55.7 at% Ge.

Annealing of this film in the TEM by focusing the beam and removing the condenser aperture resulted in the microstructure shown in Figure 4.7. SADPs from the crystallized region can be indexed according to the α -Al and β -Ge phases only (Figure 4.7b). The majority phase appears to be the β -germanium phase as would be expected from the equilibrium phase diagram. The BF/DF pair of micrographs in Figure 4.8 shows the distribution of β grains in the microstructure. The DF micrograph was taken using the portion of the ring marked with a circle in Figure 4.7b.

Previous results on Al-50Ge amorphous thin films crystallized in a similar manner showed the formation of an inner core of eutectoid($\alpha + \beta$) surrounded by an area that contained the hexagonal and orthorhombic metastable phases(27). In fact, with even more rapid heating, it was possible to produce only the hexagonal and orthorhombic phases with no eutectoid core. Thus, it was proposed that the formation of the metastable phases is favored at temperatures above where the eutectoid transformation to $\alpha + \beta$ is significant. For our sample with approximately 55 at%Ge, no evidence of metastable phase formation was found. Possible explanations for this are as follows: (i) from the previous work on the Al-30,40,50 Ge films by Kaufman et al, it has been shown that as the Ge content increased the amount of eutectoid decreased owing to the fact that as the film are enriched in Ge, the driving force for primary α -Al formation, which is easier to nucleate, decreases and the

driving force for metastable phase formation increases. Thus, a similar kinetic argument can be made for the 55 at% Ge films. At 55 at% Ge, for primary formation of the metastable phase, with the 50-50 composition, requires rejection and redistribution of Ge. If, as expected, this rejection and redistribution is difficult in these highly viscous glasses, it is conceivable that growth of the metastable phase may be sluggish or impaired allowing for the slower nucleating Ge phase to nucleate from the now Ge-enriched amorphous matrix. Following β -Ge nucleation and growth, the remaining matrix would become Al-rich resulting in the easy nucleation and growth of α -Al. Re-solution of any of primary metastable phase should then occur during the continued formation of the two stable phases. A plot of this type of transformation sequence is shown using the schematic free energy versus composition diagram in Figure 4.9. Documentation of this process is difficult from the standpoint that, in order to attempt to activate metastable phase formation, rapid crystallization is necessary which, in turn, negates the possibility of capturing the transformation as it occurs.

Another less plausible explanation concerning the absence of any metastable phases during the beam-assisted crystallization of the Al-55Ge film might be that the increase in temperature of the region being heated was not high enough to initiate metastable phase formation. As stated earlier, it was proposed by Kaufman et al(27), that

the temperature regime where metastable phases form is higher than that where the eutectoid transformation is significant. This is related to the increased kinetics available at the higher temperature and the necessity for solute redistribution between the stable α and β phases. Since it was shown by several investigators(30, 85, 86) that for metal-metalloid systems, the glass transition (as well as the crystallization temperature) increases with increasing metalloid content. Depending on the sharpness of this increase, it is plausible that at 55 at% Ge, the rise in the crystallization temperature makes it impossible to increase the temperature of a localized region of the film rapidly enough to promote metastable phase formation. While both of these scenarios seem plausible, it would appear that the kinetic argument would be more likely to occur, given the observation that in other metal-metalloid systems the magnitude of the increase in the crystallization temperature for a metalloid enrichment of 5 at% is only about 25 C, on average(29, 86).

4.2 Iron-Boron

Much like the aluminum-germanium system, the RSP of iron-boron alloys has been studied extensively. In addition, the latter alloys have met with the most commercial success due to their unique magnetic properties. In this study, the interest in the iron-boron system stems from the proposed and usually cited metastable phase diagram by Koster and Herold.

Specifically, these authors propose that the metastable Fe₃B phase forms peritectically. Examination of the equilibrium phase diagram (Figure 4.10) and the proposed metastable diagram (Figure 4.11) show some apparent inconsistencies. Since the proposal of an ordered metastable phase forming peritectically from a liquid + stable faceted phase violates our assertion that, in general, for these types of systems no equilibria exist between the metastable and stable faceted phases, a closer look at the phase selection and microstructural evolution was conducted for alloy compositions at and beyond the composition of the metastable phase. Thus, Fe-25B and Fe-27B samples were prepared and examined.

4.2.1 Fe-25B Melt Spun Ribbons

Initial XRD results from these samples showed that the majority phase present was the metastable Fe₃B orthorhombic phase with secondary α -Fe. Closer examination of the XRD results also showed two peaks that could not be indexed according to the orthorhombic Fe₃B ($\text{o-Fe}_3\text{B}$) phase or the α -Fe phase. These two peaks can be indexed to the tetragonal Fe₃B ($\text{t-Fe}_3\text{B}$) phase reported by Khan et al(87) and Das et al(88). The occurrence of both forms of the Fe₃B phase could result from two possible mechanisms. It has been proposed that the t-Fe₃B is more stable than o-Fe₃B such that, upon annealing, the $\text{o} \rightarrow \text{t}$ transformation results(12, 28). This could be accomplished through a simple re-ordering process

without the necessity for nucleation and growth of the t-Fe₃B phase. Another possibility is that the t and o phases are two distinctly different phases that happen to occupy the same compositional range and thus can both be formed depending on the processing. This would be analogous to many of the metastable phases in the Al-Ge system which show overlap in composition and which are activated through different processing treatments.

TEM of these ribbons revealed large cellular o-Fe₃B dendrites with interdendritic particles that are presumably α -Fe (Figure 4.12). No t-Fe₃B was observed in spite of the examination of many regions in the TEM, it was not possible to locate any phases that produced SAD patterns that could be indexed according to the tetragonal Fe₃B phase. SADP's from various primary particles could all be indexed according to the o-Fe₃B structure (Figure 4.13).

4.2.2 Fe-27B Melt Spun Ribbons

Examination of the equilibrium Fe-B phase diagram indicates that an Fe-27B alloy should consist of primary Fe₂B and secondary α -Fe. XRD results of the Fe-27B melt spun ribbons confirm this with the greatest number and most intense peaks corresponding to the Fe₂B phase. Assuming that the proposed diagram by Koster and Herold is correct, the presence of the Fe₃B phase might also be expected in melt spun ribbons due to the peritectic reaction L + Fe₂B-->Fe₃B. However, no peaks in XRD were found for either form

(orthorhombic or tetragonal) of the Fe₃B phase in several XRD samples taken from three batches of melt spun ribbons of this composition.

TEM examination of the microstructure of these ribbons also showed large cellular dendrites with either an interdendritic second phase or eutectic (Figure 4.14). SAD patterns taken from the primary dendrite regions can all be indexed according to zone axes of the Fe₂B phase as shown in Figure 4.15.

4.3 Discussion of Al-Ge and Fe-B Results

Previous work in the Al-Ge system on melt spun ribbons of alloys with between 5 and 50 at% Ge has shown that no equilibria exist between the four metastable phases in this system and the stable faceted β -Ge phase. Evidence in the literature shows that in most instances whenever the monoclinic metastable phase and β -Ge were found in the same microstructures they were always separated by a layer of α -Al. This can be explained by the fact that it is impossible to have the α , β , and M phases in equilibrium (i.e., with equal chemical potentials) at the same time since the free energy curves for the metastable phases must always lie above those for the stable α and β phases. Thus, this boundary layer of α -Al between the M and β -Ge phases acts to establish local equilibrium between α -Al/M and α -Al/ β -Ge with a composition gradient across the Al layer(12). Further evidence to support the suggestion of a lack of equilibrium

between the metastable and stable faceting phases was documented by Laoui and Kaufman. In their work, it was noticed that for compositions slightly enriched in Al with respect to the monoclinic metastable phase, large fractions of primary M phase were formed. For Ge-enriched compositions, however, the primary M phase was replaced by large fractions of primary β phase. From this, it was proposed that the M phase was unstable with respect to melting and that the system could lower its free energy further by re-melting any primary M phase to create a L + β mixture.

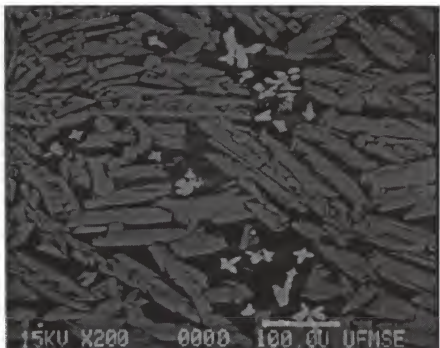
Our results for the chill splat samples of Al-48Ge and Al-52Ge agree with the previous results of Laoui and Kaufman and with their proposed mechanism that creates the differences in the observed microstructures. The results for the Al-55Ge thin film sample, however, appear somewhat inconclusive. Although the behavior is not contradictory to the reports by Laoui and Kaufman, Koster, and our chill splat results, it is difficult to determine what transformation sequence occurs during rapid crystallization of the Ge-rich film since rapid heating is required to produce the metastable phases. Slow heating of these films results in eutectoid crystallization of the stable phases which is as expected from the phase diagram at slow transformation rates where solute redistribution occurs readily since given adequate time for nucleation and growth with the necessary re-distribution of the components the stable equilibrium

phases provides the largest decrease in the free energy. Further evidence of this was shown by Laoui, who was unsuccessful in attempts to produce single metastable thin films by vapor deposition onto substrates held at temperatures where the formation of the metastable phases had occurred during liquid quenching experiments. The thermal energy provided by the substrate pre-heat and the slow rate of deposition provided the Al and Ge atoms significant time and energy to rearrange themselves into their equilibrium configurations. Thus, with the necessity for rapid heating of the film, it is not possible to detect any primary metastable phases that might have nucleated in the early stages of the transformation before its growth was pre-empted as discussed in section 4.1.

Results for the Fe-B melt spun ribbons also showed similar behavior for compositions bracketing the metastable phase. Several previous studies had alluded to the possibility of no primary Fe_3B phase being formed at boron concentrations above 25 at% B, but this had not been definitively confirmed. Clearly, our results show that at 25 at% B, the Fe_3B phase is the primary phase whereas at 27 at% B the stable Fe_2B phase is primary. It is also believed that the mechanism of re-melting of any primary metastable phase in faceting enriched compositions as proposed by Laoui and Kaufman is consistent with the present data for the Fe-B ribbons.

The metastable peritectic diagram proposed by Koster and Herold is inconsistent with the present results. In fact, examination of their diagram raises immediate questions concerning its validity. Specifically, inspection of the diagram in Figure 4.11 shows that, for the metastable peritectic reaction, the liquidus curve representing the L + Fe₂B equilibrium is inaccurate since a metastable extension must be an extension of the stable equilibrium liquidus to lower temperatures and increased compositions. In addition, barring inaccuracies in their diagram construction, an alloy with 27 at% B is expected to show the formation of the Fe₃B phase in equilibrium with the stable faceted Fe₂B phase. Since no evidence of the Fe₃B phase was found in our ribbons it can only be concluded that the diagram is inaccurate.

The diagram proposed from the present research is a metastable eutectic between α -Fe and Fe₃B as shown in Figure 4.16. Much like the diagrams proposed by Laoui and Kaufman, for compositions enriched in boron with respect to the metastable phase, metastable equilibrium between the liquid and Fe₃B phase never connects with the stable equilibria over this composition range.



(a)

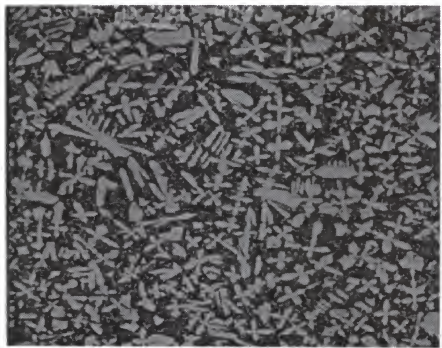


(b)

Figure 4.1. Al-48Ge chill splat backscattered SEM micrographs.



(a)



(b)

Figure 4.2. Al-52Ge chill splat backscattered SEM micrographs.

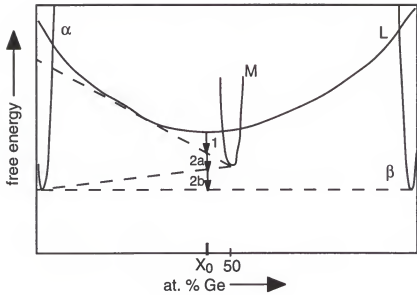


Figure 4.3. Schematic Free Energy curves depicting the transformation sequence in an Al-48Ge chill splat.

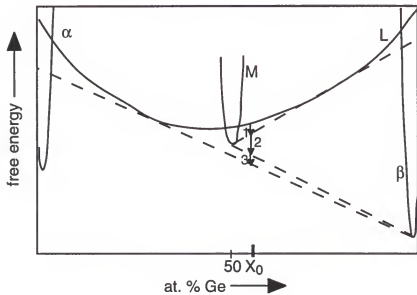


Figure 4.4. Schematic Free Energy curves depicting the transformation sequence in an Al-52Ge chill splat.

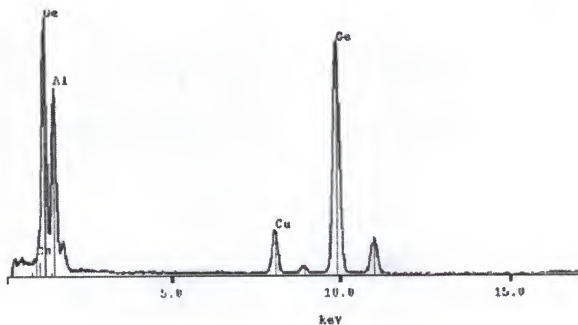


Figure 4.5. EDS spectrum from a monoclinic phase in an Al-36Ge ribbon.

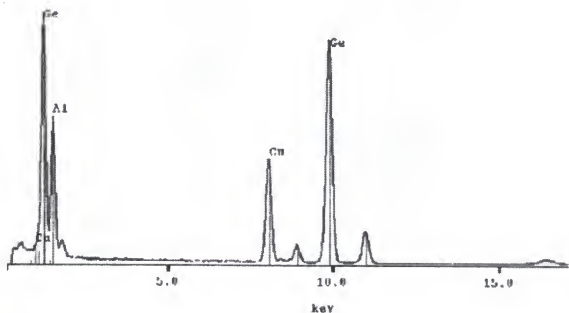


Figure 4.6. EDS spectrum from Al-Ge thin film.

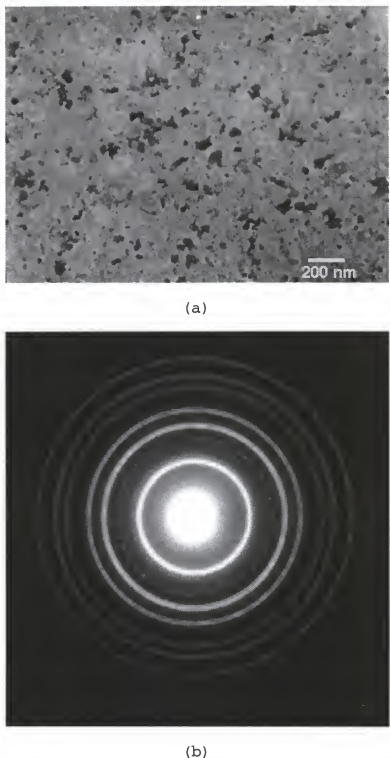
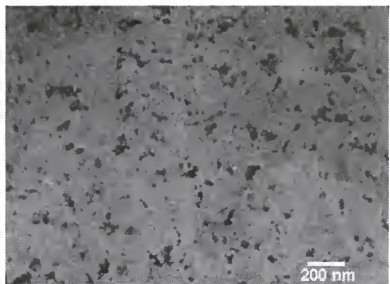
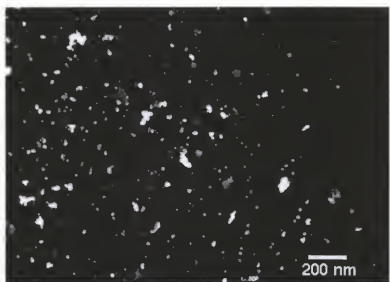


Figure 4.7. Crystallized Al-Ge (a) Bright Field image (b) SAD ring pattern.



(a)



(b)

Figure 4.8. Al-Ge crystallized film (a) BF (b) DF from first ring in figure 23.

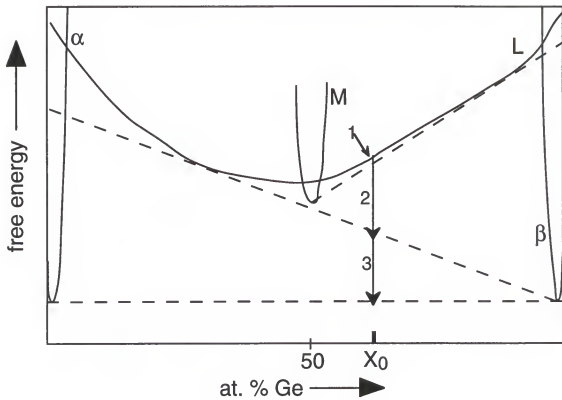
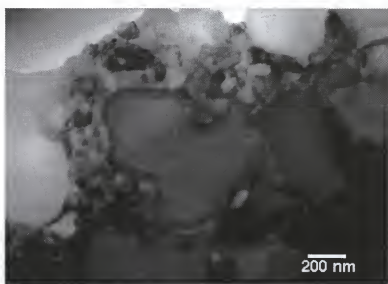
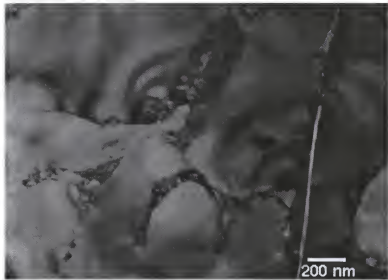


Figure 4.9. Schematic Free Energy showing the possible reaction path for the "shut-down" mechanism proposed for an Al-55Ge thin film.

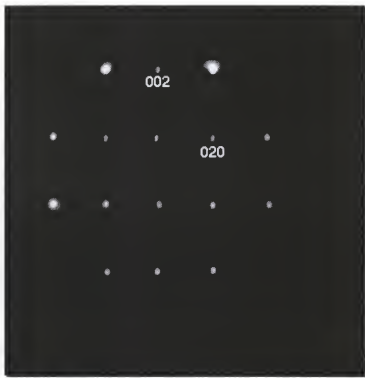


(a)



(b)

Figure 4.10. BF micrographs from Fe-25B ribbon showing cellular Fe-3B(O) phase and interdendritic regions.

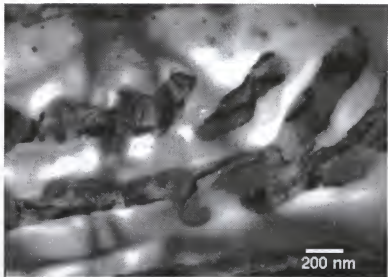


(a)



(b)

Figure 4.11. SAD patterns from an Fe-25B ribbon (a) $B=[00\bar{1}]$
(b) $B=[22\bar{1}]$.

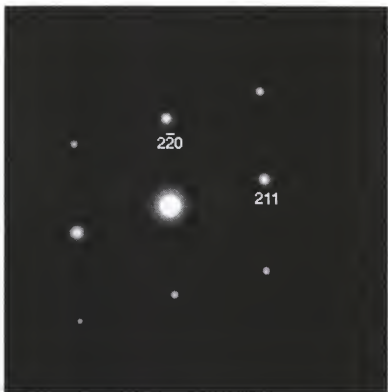


(a)

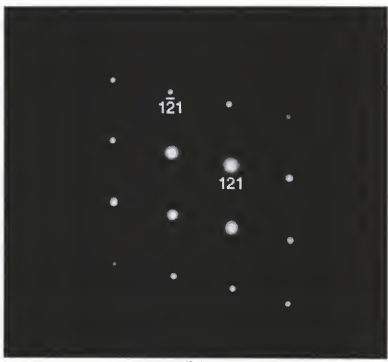


(b)

Figure 4.12. BF micrographs from Fe-27B ribbon showing cellular Fe-3B(O) phase and interdendritic regions.



(a)



(b)

Figure 4.13. SAD patterns from Fe-27B ribbons (a) $B=[10\bar{1}]$ and (b) $B=[11\bar{3}]$

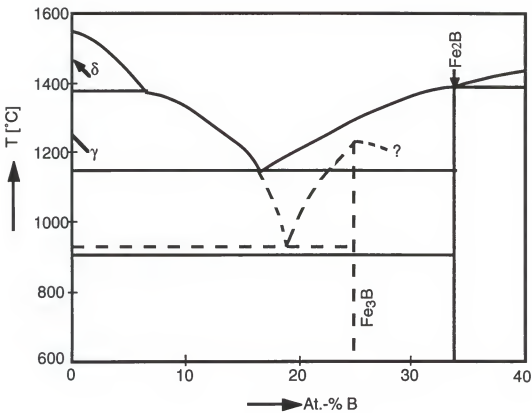


Figure 4.14. Metastable Eutectic phase diagram ($L \rightarrow a\text{-Fe} + \text{Fe}_3\text{B}$) as proposed from present research.

CHAPTER 5 HAFNIUM-BERYLLIUM RESULTS AND DISCUSSION

5.1 RESULTS

As a result of the numerous experimental techniques used to characterize the phase transformations and microstructural evolution of hafnium-beryllium metallic glass ribbons, this chapter will be divided into four distinct sections as follows: (i) X-ray diffraction of bulk annealed samples, (ii) high temperature x-ray diffraction, (iii) TEM of bulk annealed samples, and (iv) in-situ transformations using a hot stage in the TEM.

5.2 XRD of Bulk Annealed Samples

XRD of annealed melt spun ribbons was undertaken as a means of identifying the phases present following bulk crystallization anneals. While this technique of phase determination is valuable, it does have two major limitations, namely: (i) no information concerning the mechanism of microstructural evolution can be definitively discerned and (ii) this technique is limited to identifying phases that are sufficiently large and occur in fairly large volume fractions (>5%) (89, 90). Even so, XRD thus provides a good overall picture of the majority phases present following a prescribed annealing/processing treatment

5.2.1 X-Ray Diffraction of Hf-45Be Bulk Annealed Samples

Figure 5.1 shows the XRD pattern for an Hf-45Be specimen annealed at 500 C for 15 minutes. Overall, the plot appears featureless with two small peaks above background appearing at approximately 30 and 35.5 degrees. The corresponding d-spacings for peaks at those angular positions are $d_1=0.298\text{nm}$ and $d_2=0.253\text{nm}$. A comparison of these two d-spacings with the JCPDS cards for α -Hf (hcp), metastable m-HfBe, and HfBe₂ phases reveals that the 0.298nm spacing corresponds most closely to the spacing of the (021) planes of the m-HfBe phase. The 0.253nm spacing, however, could result from either α -Hf or m-HfBe. Examination of the relative intensities for these two phases reveals that the peak corresponding to the 0.253nm spacing must correspond to the m-HfBe phase since the stronger peaks from a-Hf were not observed.

The XRD pattern from the Hf-45Be ribbon after annealing at 500 C for 30 minutes, contained numerous peaks indicating more complete crystallization of the amorphous structure (Figure 5.2). This plot contains approximately 10 peaks clearly above the background with possibly four more perturbations above background that may correspond to actual peaks. The majority phase following this annealing treatment is clearly the metastable m-HfBe phase. The approximate metastable phase diagram in Figure 5.3 can be used to estimate the volume fraction of the m-HfBe and a-Hf phases as 91% and 9% respectively.

Results from longer annealing treatments (500 C for 45 minutes) are consistent with these data.

5.2.2 X-ray Diffraction of Hf-50Be Bulk Annealed Samples

Bulk furnace anneals of Hf-50Be ribbons at 500 and 525 C for times from 15 to 65 minutes show evidence to support Tanner's assertion of polymorphic crystallization for ribbons of this composition. For a sample heated at 500 C for 15 minutes (Figure 5.4) only five peaks are clearly above background and these peaks correspond to the following d-spacings: 0.297, 0.241, 0.235, 0.155, and 0.145 nm. According to Tanner's calculated d-spacings for the metastable m-HfBe phase with an orthorhombic crystal structure isotypic with CrB (Cmcm space group), all of these peaks can be attributed to this phase. Samples annealed at the same temperature for longer times once again show peaks only from the metastable phase; as the time was increased to 65 minutes (Figure 5.5), the five original peaks from the 15 minute sample all increased in magnitude and additional peaks from this phase were observed. The increase in the number of peaks indicates that the ribbons are approaching complete crystallization with crystallites of many different orientations being formed. Also, the development of peaks at many different orientations demonstrates the lack of a preferred orientation or texture developing during crystallization.

The Hf-50Be specimens annealed at 525 C for 15 and 30 minutes decompose in a similar manner to those at 500 C except at a slightly higher rate.

5.2.3 X-Ray Diffraction of Hf-55Be Bulk Annealed Samples

Hf-55Be samples were initially annealed at 500 and 525 C for times from 15 to 30 minutes. The specimen annealed at 500 C for 15 minutes contained peaks consistent with the HfBe₂ and α -Hf phases (Figure 5.6). There are clearly more and larger (higher intensity) peaks corresponding to the stable intermetallic phase (HfBe₂) indicating a larger amount of this phase being present. The equilibrium phase diagram indicates that, for an alloy with 55 at% Be, the majority phase should be HfBe₂ at approximately 82 vol.% with the remaining 18% being α -Hf assuming that the amorphous structure was completely transformed. Tables 2 and 3 show the results for samples annealed at the same temperature for 20 and 30 minutes, respectively. Once again, the peaks detected by XRD correspond to the HfBe₂ and α -Hf phases with the HfBe₂ phase appearing to be the majority phase.

It should be noted that for these 15 minute furnace anneals, it was not possible, to isolate which of these phases was the primary phase during crystallization. Thus, in an attempt to ascertain the primary phase of crystallization in ribbons with 55 at% Be, samples were annealed at 500 C for 8 and 12 minutes. The samples annealed for 8 minutes had an XRD plot that was completely featureless except for the characteristic broad intensities associated

with the amorphous structure. However, an unexpected result occurred in the sample annealed for 12 minutes; namely, that equilibrium phases an additional two peaks were present that were indexed as the second and third most intense peaks of the metastable m-HfBe phase (Figure 5.7). Since none of the samples held at longer annealing times showed evidence of this metastable phase, it would appear that the m-HfBe phase might be the first phase to nucleate from the amorphous structure before decomposing into the stable phases.

5.3 TEM of Bulk Annealed Samples

Examination of the microstructure in these Hf-Be metallic glass ribbons following annealing allows for the determination of the crystallite size and shape, possible mechanism of the transformation, and helps build the picture of phase selection/microstructural evolution in these materials. In addition, TEM affords the opportunity to confirm the phases present in the XRD patterns and to document any previously undetected phases.

5.3.1 TEM of Hf-45Be Bulk Annealed Samples

Hf-45Be samples annealed at 500 C for 30 minutes showed a mixture of α -Hf and m-HfBe in XRD plots. TEM analysis (Figure 5.8) revealed fine (50-100nm) grain crystallization structures consisting of α -Hf and m-HfBe. Due to the fact that by 30 minutes, complete crystallization of the amorphous starting structure occurred, it was impossible to discern which of the two phases was the first phase to nucleate upon

crystallization. Figure 5.9 shows SADP ring diffraction patterns from two different regions in the sample annealed for 30 minutes. Figure 5.9(a) shows a ring pattern from one of the regions that can be indexed solely according to Tanner's structure and lattice parameters for the metastable m-HfBe phase. This analysis must be qualified however, since the two major reflections or sets of diffracting planes for both the metastable m-HfBe phase and the α -Hf phase occur at similar d-spacing. This means that one cannot unequivocally state that the microstructure consists solely of m-HfBe. However, the ring pattern displayed in Figure 5.9(b) taken from another region in the same TEM foil shows clear evidence of the α -Hf phase. Examination of the JCPDS card for hcp hafnium shows that the three most intense peaks/reflections occur, (from highest to lowest) at d-spacings of 0.243, 0.253, and 0.277 nm. Determination of a proper indexing scheme for this ring pattern shows that the fourth ring out from the central transmitted spot corresponds to a d-spacing of 0.2768nm, showing that α -Hf is clearly present in this region of the foil.

5.3.2 TEM of Hf-50 Be Bulk Annealed Samples

TEM of bulk annealed Hf-50Be samples was performed not only to confirm the presence of the m-HfBe phase as detected by XRD but also to provide confirmation of the proposed crystal structure and space group for this phase. Tanner proposed an orthorhombic crystal structure with the Cmcm space group and the following lattice constants, $a=0.334$,

$b=1.00$, and $c=.372$ nm. Figure 5.10 shows the microstructures of a sample heated at 500 C for 15 minutes. Ring patterns from this sample can be indexed according to Tanner's structure for the m-HfBe phase. It is interesting to note that even after 30 and 45 minutes at this temperature, complete crystallization did not occur as displayed in Figure 5.11. Thus, for Hf-50Be samples subjected to the aforementioned heat treatments the resulting structure is simply primary m-HfBe in an amorphous matrix.

Examination of the change in size of the m-HfBe crystallites with time (Figure 5.12) can provide information concerning the growth of this phase. As seen in these micrographs, the coarsening of the metastable phases in ribbons of this composition is rather slow. In fact, by 45 minutes as shown the consumption of the amorphous matrix is just approaching completeness.

5.3.3 Confirmation of Crystal Structures for m-HfBe

Although the aforementioned XRD and TEM results agree with Tanner's calculated peak positions/d-spacings, it was still necessary to investigate if the orthorhombic structure with a Cmcm space group as proposed was correct since it is possible to devise numerous structures with different lattice parameters that could provide similar d-spacings. The most appropriate method to perform structure and space group determination is by using convergent beam electron diffraction (CBED) in the transmission electron

microscope(91). CBED relies on a convergent electron probe instead of a parallel beam of illumination as used in conventional SAD diffraction analysis. As a result of the incident electron beam not being parallel, the diffraction information is in the form of disks rather than spots and these disks can be used to gather information concerning the symmetry of the crystal structure.

Hf-50Be specimens containing primary m-HfBe crystallites in an amorphous matrix were used for the structure analysis determination. As can be seen in Figure 5.13, the CBED patterns from this phase are rather poor, and contain little symmetry information presumably due to internal strain and defects in the transformed crystallites. Further attempts at CBED were unsuccessful and, although some useful information was obtained, the quality of the patterns was insufficient to allow for the requisite symmetry analysis. As a result, it was necessary to generate SADP's from several crystallites with this structure and to map out the reciprocal lattice for this phase (Figure 5.14). In order to properly index each zone axis pattern and determine its relationship to the other zones, determination of the angles between each zone was performed by recording the goniometer tilt angles. This made it possible to index the pattern on the basis of an orthorhombic system with $a=0.372$, $c=1.00$, and $c=0.334\text{nm}$. Confirmation of the space group assigned by Tanner was performed by examining the patterns and documenting the occurrence of allowed and forbidden reflections according to

the Pearson's Table(92) for the Cmcm space group. If any forbidden reflections were documented, care was taken to locate a double diffraction path that would be responsible for that reflection. Based on this analysis, it is possible to assign the Cmcm space group to the metastable m-HfBe phase as proposed by Tanner.

5.3.4 TEM of Bulk Annealed Hf-55Be Samples

Hf-55Be samples annealed at 500 C for times from 12 to 30 minutes show what is believed to be primary m-HfBe at shorter times and a mixture of α -Hf and HfBe₂ at longer times. Figure 5.15 shows bright field micrographs and the corresponding ring patterns for the sample annealed for 12 minutes. Typically, these are fine grain (50-75nm) structures consisting of m-HfBe and HfBe₂. Indexing the ring pattern taken from their respective regions shows that the only two phases present in this sample are the m-HfBe and HfBe₂ phases. The only major discrepancy concerns the ring corresponding to a d-spacing of 0.241nm. Both the m-HfBe and α -Hf phases have major reflections at this spacing so it is difficult to unequivocally state that no α -Hf is present. In order to determine the nature of the co-existence of the metastable phase and the stable faceted phase within this microstructure attempts were made to perform dark field TEM in order to determine the position of these two phases with respect to each other. Due to the scale of the as crystallized microstructures, the only success with these

efforts was to determine which phases in the fine grained microstructure were the stable HfBe₂ phase.

Hf-55Be samples annealed for 15 (Fig 5.16) and 30 (Fig 5.17) minutes exhibited crystallization microstructures that were quite different in appearance and phases present with respect to the 12 minute anneal. The 30 minute annealed structure is slightly coarser structure than that at 15 minutes and the SADP ring patterns from different regions of this foil show more or less rings that can be attributed α -Hf as shown in Figure 5.17. This is most likely due to fewer grains being used to generate the pattern in the coarser sample compared to the less coarse 15 minute anneal for the same size selected area aperture.

5.4 In-Situ XRD and TEM Studies of Hf-Be Ribbons

The in-situ (real-time) TEM and XRD investigations of these metallic glass ribbons were performed in an attempt to document the reaction sequences as they occur in order to provide some insight into the mechanisms of devitrification. These methods are complementary since high temperature XRD provides a more macroscopic picture of the transformation sequences while TEM allows reexamination on a micro-scale.

5.4.1 High Temperature XRD of Amorphous Hf-Be Ribbons

In situ, high temperature XRD was performed on Hf-50Be ribbon samples in order to (i) confirm the previous bulk

post-annealing results and (ii) to examine the decomposition behavior of the m-HfBe phase. For the Hf-50Be alloy, samples were heated at 20°C/min from room temperature to 490° C and then taking XRD scans were taken at 10° from 490-640° C (Figure 5.18). Clearly, the metastable m-HfBe phase nucleates in this sample as expected. Upon continued heating to 560°C, the major peaks for the m-HfBe phase over the angular range scanned (26 to 40), all appear and increase in magnitude indicating that the sample undergoes complete crystallization to this phase. At approximately 560°C the peaks corresponding to (110), (021), and (111) are at their maximum intensities. A scan taken at 570 C shows a decrease in the intensity of these peaks and the appearance of new peaks that can be indexed according to the stable HfBe₂ phase. Continued heating to 600 C shows the further decrease in the intensity of the primary m-HfBe peaks and increasing intensity of the HfBe₂ peaks along with the appearance of new peaks that can be indexed according to the α -Hf phase. At 640C all of the peaks present can be indexed according to HfBe₂ and α -Hf with the HfBe₂ phase as the majority.

High temperature XRD of the Hf-45Be sample was performed in an attempt to identify definitively whether primary or eutectoid crystallization occurred. Bulk post-annealling XRD results suggested primary m-HfBe formation but were somewhat inconclusive. As before, the samples were heated to 480 C at 20C/min and then XRD scans were taken every 10 to 640C. Once again, it is difficult to surmise whether or not primary or

eutectoid crystallization occurred. The XRD plot in Figure 5.19 shows that at 490 C evidence of peaks corresponding to both phases are present which might lead one to conclude that eutectoid crystallization had occurred. However, since there is some time lag between scans it is possible that primary crystallization occurred followed by the subsequent nucleation and growth of the secondary phase. Nevertheless, it is quite clear that the majority phase in these ribbons is the m-HfBe phase. Continued heating to approximately 570 C results in the beginning of the transformation of the metastable phase into the two stable phase. Further heating as shown in Figure 5.19, promotes the complete decomposition of the metastable phase into the stable α -Hf and HfBe₂ phases.

Heating of an Hf-55Be sample in a manner similar to the Hf-45Be ribbon in the high temperature X-ray diffractometer results in primary crystallization of the metastable m-HfBe phase by 510 C. Transformation of this phase resulting in a mixture of the two stable phases (α -Hf + HfBe₂) results by 530 C. Further heating to 600 C increases the intensity of the peaks from the two stable phases.

5.4.2 In-situ TEM Hot Stage Microscopy

In-situ TEM hot stage microscopy affords the opportunity to visually examine the crystallization of amorphous ribbons in real time and to document the sequence of microstructural development. The one drawback to solely relying on this

technique for studies of microstructural evolution is the criticism that transformations occurring in thin (150–200nm) TEM foils may not be representative of the bulk material.

For the Hf-45Be samples heated in-situ, primary m-HfBe formation (Figure 5.20) followed by the subsequent appearance of secondary α -Hf was observed. The SAD patterns shown in Figure 5.21 confirm that the primary phase is indeed m-HfBe. Further annealing at 515 C reveals a complex, two-phase microstructure with the m-HfBe phase being of the order of 50–75nm as seen in Figure 5.22. SAD ring patterns of this two-phase structure can be indexed according to the α -Hf and m-HfBe phases. The appearance of more and stronger rings from the m-HfBe phase demonstrates that the m-HfBe phase is the majority phase as would be expected from examination of the proposed metastable phase diagram (Figure 5.3). Further heating to examine the decomposition of the m-HfBe phase was carried out for samples of this composition and this issue will be addressed subsequent sections.

Figure 5.23 displays the primary crystallization structure typical of an Hf-50Be sample heated in-situ. The ring patterns in Figure 5.23b taken from the collection of crystallites could all be indexed according to the m-HfBe phase. Further heating of the Hf-50Be sample resulted in the transformation of the metastable phase into the two stable phases as shown in Figure 5.24.

Analogous to the bulk ribbon results, the first phase to develop in Hf-55Be is primary m-HfBe (Figure 5.25). With

continued heating this phase rapidly transforms into the stable mixture of α -Hf and HfBe₂ (Figure 5.26).

Following these initial in-situ experiments, it was decided that in order to attempt to make a definitive statement concerning the nature of the equilibrium between the metastable phase and the HfBe₂ phase, close examination of the decomposition reaction in ribbons with each composition was imperative. Since primary metastable phase formation for compositions enriched in the faceting component (Be) with respect to the stoichiometry of the metastable phase has been documented via XRD and TEM, the issue of whether or not HfBe₂ and m-HfBe ever come into contact is raised. If these two phases are observed to be in contact, it could mean that a local equilibrium might exist between them. However, one issue to be addressed is that of whether the stable phase can nucleate on the metastable phase (thus being in contact) without the necessity for local equilibrium, i.e., with the necessity for equilibrium arising only when the stable phase attempts to grow and consume the metastable phase. It was these concerns that lead to the attempt to examine the decomposition phenomenon as described in the following section.

5.4.3 Transformation of the m-HfBe Phase

An Hf-55Be sample was heated in-situ to the point where decomposition of the m-HfBe phase had just begun. The SADP's displayed in Figure 5.27 show intense streaking and spot

broadening indicating the beginning of the decomposition process. Examination of the microstructure at this stage (Figure 5.28) shows the m-HfBe phase with a "brush stroke" appearance. Further heating led to the sequence of SADP's which document the decomposition process in real time (Figure 5.29). From Figure 5.29, we see that as new reflections appear during the decomposition they are randomly dispersed and show no evidence of an orientation relationship. In fact, close examination of Figure 5.29(h) shows what appears to be remnants of the original m-HfBe zone axis pattern with faint rings from the two stable phases in the background. Further evidence of a lack of orientation relationship is shown in Figure 5.30, where SADP's from other m-HfBe crystallites undergoing a transformation with ring patterns from the two stable phases also appearing. The microstructure at this stage of heating consists of a fine two phase mixture of α -Hf and HfBe₂ with small regions of the original m-HfBe phase still undergoing decomposition.

5.5 Discussion of the XRD and TEM Results

Examination of both the XRD and TEM data for the Hf-Be samples with between 45 and 55 at% Be show consistent results between the more macroscopic XRD data and the microscopic TEM data. It is possible to rationalize the transformation sequences that would account for the observed XRD and TEM data by employing hypothetical free energy versus composition diagrams. Since metastable phases have the same

characteristics as stable phases it is possible to discuss their thermodynamic properties (heat capacity, heats and entropies of fusion, and Gibbs free energy) in the same context as stable phases. Thus, it is possible to use standard free energy curve constructions and draw common tangents at particular temperatures in order to determine the metastable phase compositions in local equilibrium with other metastable phases, stable phases or the liquid/amorphous phase. However, as noted previously, any truly quantitative treatment requires knowledge concerning the thermochemical properties of the metastable phase which are difficult to measure experimentally due to the difficulty in producing the metastable phase in bulk form. Schematic free energy constructions are useful, however, for elucidating the behavior of metastable phases that form competitively with stable phases. For the Hf-Be system, it should be duly noted that certain assumptions have been made concerning the shape and position of the respective curves in this construction.

The devitrification reactions for metallic glass ribbons with 45 at% Be were documented by both XRD and TEM to occur as follows:



Figure 5.31 shows a plot of Gibbs free energy versus composition with the following transformation sequences documented as sequence I, II, and III. In sequence I,

primary m-HfBe nucleates from the amorphous phase with concomitant hafnium enrichment of the amorphous matrix. With this enrichment, the driving force for α -Hf increases resulting in the complete metastable crystallization of the samples. As shown through high temperature XRD, further heating results in sequence III with the decomposition of the m-HfBe phase into the two stable phases.

For ribbons of equiatomic composition, XRD and TEM results suggest the polymorphic crystallization reaction depicted in Figure 5.32 as sequence I. The polymorphic reaction results in the formation of m-HfBe with no apparent compositional change. It is interesting to note that for ribbons of this composition in bulk annealings at 500C for times up to 65 minutes the only phase detected was the m-HfBe phase. If we assume that complete crystallization has occurred in 65 minutes, the thermal stability of the metastable m-HfBe phase is quite good alluding to the possibility that the free energy curve for the m-HfBe phase may be only slightly above those for α -Hf and HfBe₂.

The most complex of the documented devitrification reactions results during the crystallization of ribbons containing 55 at% Be. XRD and TEM results for a sample annealed 500 C for 12 minutes showed a mixture of m-HfBe and HfBe₂. Since none of the samples held for time longer than 12 minutes showed m-HfBe formation it was decided that in the 12 minute sample, the m-HfBe phase present must be the primary phase with the HfBe₂ being secondary or as a result

of decomposition. This was confirmed with high temperature XRD and in-situ TEM where it was shown that the primary phase was indeed the m-HfBe phase and that decomposition did occur rather quickly into a mixture of the two stable phases.

Examination of the schematic free energy versus composition diagram for an alloy with this composition reveals that primary m-HfBe formation should result in the enrichment of the amorphous matrix in beryllium as a result of the solute rejection during growth (Figure 5.33). This provides a large driving force for the formation of HfBe₂. It is interesting to note the disparity in the thermal stability of the m-HfBe phase in an alloy with this composition compared to that of an alloy with 50 at% Be. It has been shown in Fe-B alloys that diffusion even in metallic glass systems is considerably slower than even solid state diffusion in the crystalline phase(on the order of 10^{-18} - 10^{-22} m²s⁻¹ near T_g)^(63, 71, 93, 94, 95, 96, 97, 98, 99) as a result of the increased viscosity of the liquid with increasing undercooling. Thus, if it is difficult for the rejected beryllium to diffuse away from the m-HfBe nuclei and a build up of solute occurs significant growth after nucleation of the m-HfBe phase will be precluded; the Be enriched material surrounding the m-HfBe will thus possess a large driving force for HfBe₂ nucleation. If HfBe₂ nucleates in these Be-enriched regions it will reject hafnium in order to grow which will then shift the remaining matrix composition toward hafnium enrichment and ultimately result

in α -Hf nucleation. This scenario would explain the difference in the phases present in the 55 at% Be samples annealed for 12 and 15 minutes. The absence of any XRD peaks or SAD rings from the m-HfBe phase in the sample annealed for 15 minutes would suggest a transformation to the two stable phases.

The proposed behavior in the Be-rich Hf-Be alloys appears to be consistent with the explanation of the behavior in the Al-Ge work by Laoui and Kaufman. For this case, alloys enriched with respect to the stoichiometry of the metastable phase showed primary β -Ge and either stable or metastable eutectic in their final microstructures. However, it was proposed that the true primary phase on cooling from the liquid was the metastable monoclinic phase. Throughout the use of the schematic free energy curves shown in Figure 2.3, they proposed a reaction sequence for cooling from the liquid that seems analogous to the mechanism proposed for our Hf-Be ribbons with 55 at% Be. Thus it would seem logical to propose a metastable eutectic diagram as shown in Figure 5.34 between α -Hf and the m-HfBe phase. This type of diagram is not without precedent since a previous phase diagram calculation of TM-Be systems by Kaufman and Tanner(100, 101) indicated that, for the Ti-Be system, the metastable diagram contained a eutectic between α -Ti and the m-TiBe phase.

The results from the XRD and TEM samples suggest the presence of a metastable eutectic invariant between m-HfBe and α -Hf as shown in Figure 5.34. However, in order to

provide conclusive evidence, especially in the 55 at% Be samples, in-situ TEM studies of the decomposition of the m-HfBe phase were performed. Examination of the decomposition reaction showed that the m-HfBe phase transforms at increased temperatures to a mixture of a-Hf and HfBe₂. SADP's taken during the decomposition showed no orientation relationship between the m-HfBe and the stable phases. The mechanism of the decomposition process remains unclear due to the speed at which the reaction occurs and also the fine scale of the resulting microstructure. Even so it is clear that the mechanism does not involve a displacive phase transformation from the m-HfBe phase to the HfBe₂. This issue was raised because, according to Pearson(102), the structure of m-HfBe can be shown to be a crystallographica derivative of the HfBe₂ structure. HfBe₂ is isotypic with AlB₂ and possesses an hexagonal (hP3) arrangement of its atoms as shown in Figure 5.35. From Pearson(102), the CrB (oC8) structure of m-HfBe can be produced from the AlB₂ structure by simply displacing the layered structure of AlB₂ by $a/2$ and $c/2$ (Figure 5.36). Thus, while it might be suggested that the decomposition of m-HfBe might occur by a displacive mechanism involving the coordinated movement of the atoms the SADP's recorded during decomposition displayed no evidence for an orientation relationship (OR) and, therefore, this mechanism is not operative. Furthermore, since no OR was observed between these phases it would appear that no type of

precipitation or decomposition mechanism existed between these phases.

Lastly, while a displacive ($m\text{-HfBe} \rightarrow \text{HfBe}_2$) mechanism of decomposition can be ruled out, the true mechanism for decomposition could not be discerned. Although, no clear evidence was documented showing that the $m\text{-HfBe}$ and HfBe_2 phases are in local equilibrium, the nature of the equilibria between them remains inconclusive. Discovery of the true operative mechanism was hindered by the speed with which the reaction occurred and also due to the fine scale of the transforming microstructure and therefore, our assertion of the generality of the behavior between MOP's and stable faceting phases is still intact. No conclusive evidence has been documented showing a MOP and stable faceting phase to be in equilibrium for three such faceted/non-faceted systems and thus it is still believed that for faceted/non-faceted systems no metastable phase equilibria exist experimentally between MOP's and stable faceting phases.

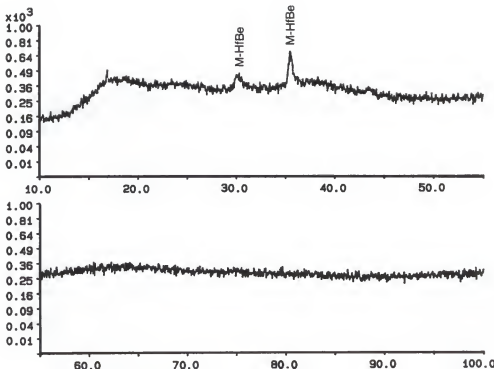


Figure 5.1. XRD plot of Hf-45Be annealed at 500°C for 15 min.

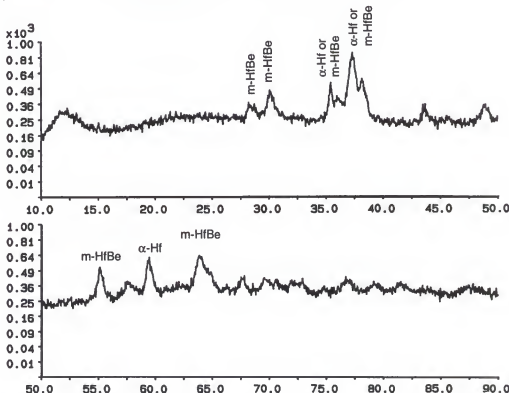


Figure 5.2. XRD plot of Hf-45Be annealed at 500°C for 30 min.

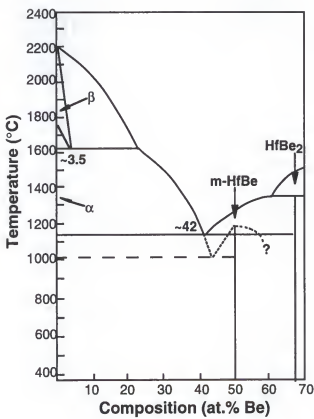


Figure 5.3. Metastable Phase Diagram for Hf-Be as proposed from present research.

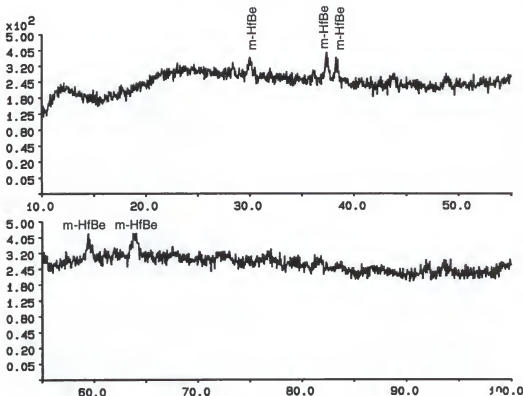


Figure 5.4. XRD plot of Hf-50Be annealed at 500°C for 15 min.

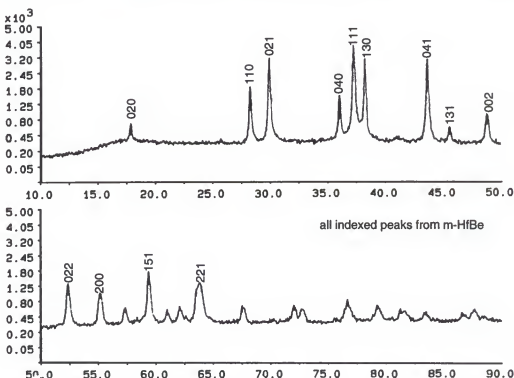


Figure 5.5. XRD plot of Hf-50Be annealed at 500°C for 65 min.

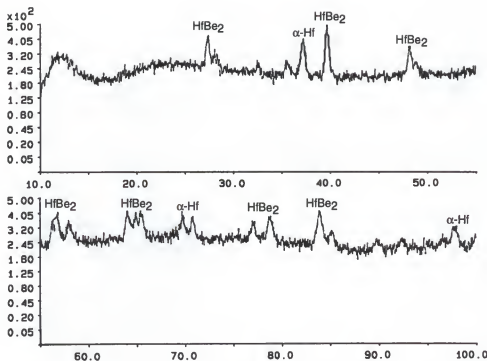


Figure 5.6. XRD plot of Hf-55Be annealed at 500°C for 15 min.

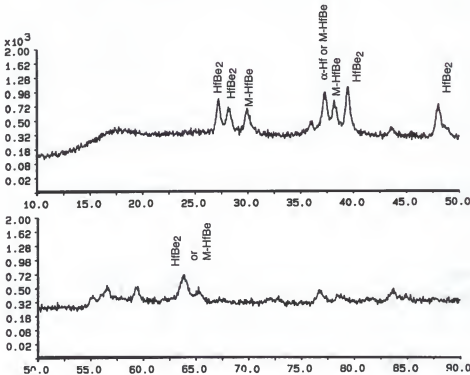


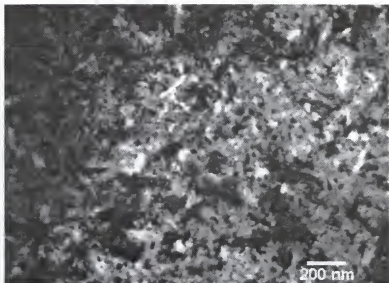
Figure 5.7. XRD plot of Hf-55Be annealed at 500°C for 12 min.

Table 5.1. XRD data for an Hf-55Be annealed at 500°C for 20 min.

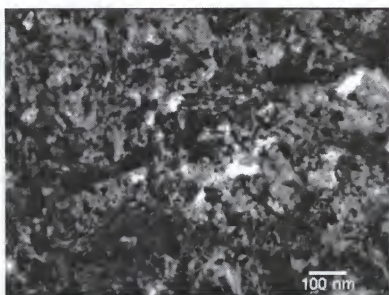
| Angle | D-Spacing (Å) | I/I _{max} | Phase |
|---------|---------------|--------------------|-------------------|
| 27.2525 | 3.2697 | 71 | HfBe ₂ |
| 28.1775 | 3.1644 | 27 | HfBe ₂ |
| 32.4775 | 2.7546 | 12 | Hf |
| 35.5200 | 2.5253 | 16 | Hf |
| 37.1125 | 2.4205 | 57 | Hf |
| 39.5700 | 2.2757 | 100 | HfBe ₂ |
| 48.0550 | 1.8918 | 41 | HfBe ₂ |
| 56.0125 | 1.6404 | 17 | HfBe ₂ |
| 56.6325 | 1.6239 | 33 | HfBe ₂ |
| 57.7025 | 1.5964 | 15 | Hf |
| 63.8875 | 1.4559 | 25 | HfBe ₂ |
| 65.3500 | 1.4268 | 22 | HfBe ₂ |
| 69.5950 | 1.3498 | 11 | Hf |
| 70.5975 | 1.3331 | 10 | Hf |
| 75.1275 | 1.2635 | 2 | Hf |
| 76.9075 | 1.2387 | 13 | HfBe ₂ |
| 78.5800 | 1.2164 | 14 | HfBe ₂ |
| 83.6725 | 1.1549 | 20 | HfBe ₂ |
| 85.0925 | 1.1392 | 8 | HfBe ₂ |
| 89.4700 | 1.0944 | 4 | HfBe ₂ |
| 92.2875 | 1.0683 | 4 | Hf |
| 96.3050 | 1.0341 | 5 | HfBe ₂ |
| 97.6350 | 1.0235 | 6 | Hf |

Table 5.2. XRD data for an Hf-55Be annealed at 500°C for 30 mins.

| Angle | D-Spacing (Å) | I/I _{max} | Phase |
|---------|---------------|--------------------|-------------------|
| 27.1550 | 3.2812 | 77 | HfBe ₂ |
| 28.2150 | 3.1603 | 14 | HfBe ₂ |
| 32.4000 | 2.7610 | 12 | Hf |
| 35.5300 | 2.5246 | 17 | Hf |
| 37.0825 | 2.4224 | 64 | Hf |
| 39.5525 | 2.2767 | 100 | HfBe ₂ |
| 48.8600 | 1.8900 | 43 | HfBe ₂ |
| 56.6550 | 1.6234 | 48 | HfBe ₂ |
| 57.8675 | 1.5922 | 26 | Hf |
| 63.8825 | 1.4560 | 49 | HfBe ₂ |
| 65.3300 | 1.4272 | 38 | HfBe ₂ |
| 69.5725 | 1.3502 | 28 | Hf |
| 70.6650 | 1.3320 | 20 | Hf |
| 76.8500 | 1.2394 | 20 | HfBe ₂ |
| 78.7200 | 1.2146 | 33 | HfBe ₂ |
| 83.6625 | 1.1550 | 37 | HfBe ₂ |
| 84.9425 | 1.1408 | 19 | HfBe ₂ |
| 89.7000 | 1.0922 | 8 | HfBe ₂ |
| 92.2575 | 1.0685 | 11 | Hf |
| 96.3300 | 1.0339 | 10 | HfBe ₂ |
| 97.7375 | 1.0227 | 19 | Hf |



(a)



(b)

Figure 5.8. Bright Field micrographs of an Hf-45Be sample annealed at 500°C for 30 min. (a) at 50K (b) at 100K.

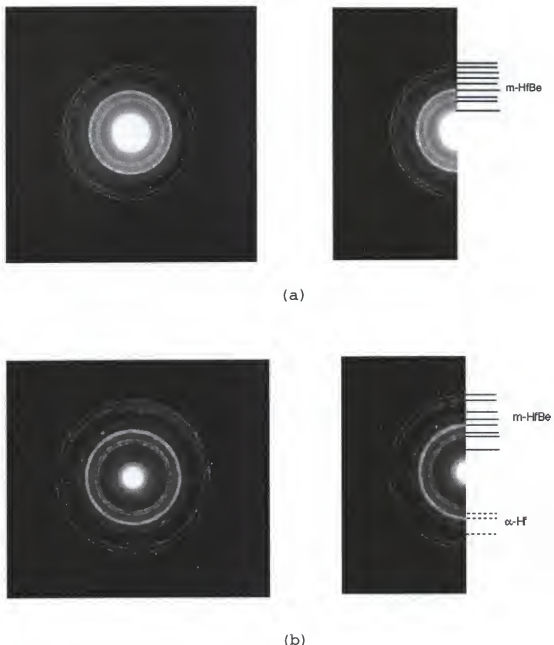
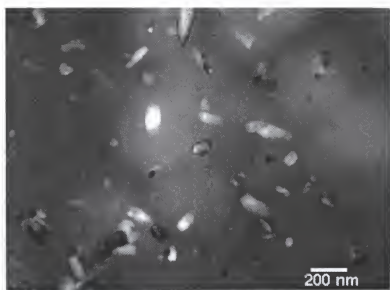
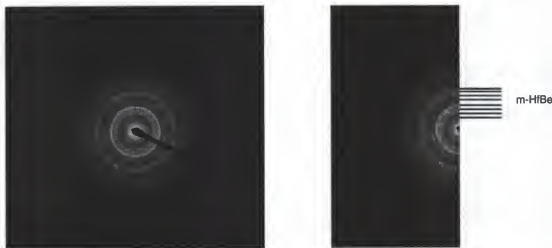


Figure 5.9. SAD Ring Patterns from Hf-45Be sample annealed at 500°C for 30 min. (a) m-HfBe rings only (b) m-HfBe+ α -Hf rings.

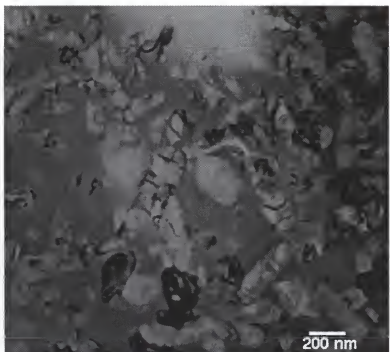


(a)

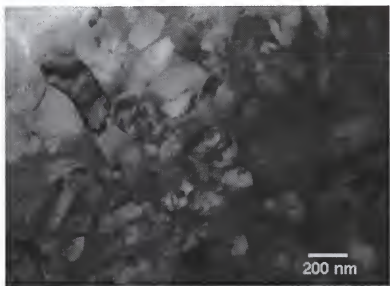


(b)

Figure 5.10. Hf-50Be annealed at 500°C for 15 min. (a) Bright Field micrograph of amorphous+m-HfBe crystallites (b) SAD ring pattern from (a).



(a)



(b)

Figure 5.11. Hf-50Be annealed at 500°C (a) 30 min. (b) 45 min.

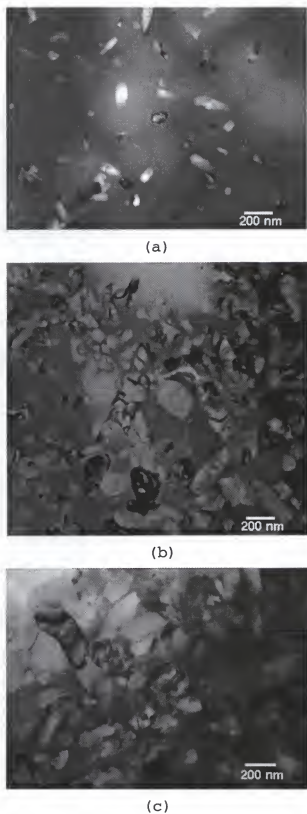


Figure 5.12. Coarsening of m-HfBe crystallites at 500°C
(a) 15 min (b) 30 min (c) 45 min.



(a)



(b)

Figure 5.13. CBED patterns from m-HfBe crystallites
(a) $B=[102]$ (b) $B=[011]$.

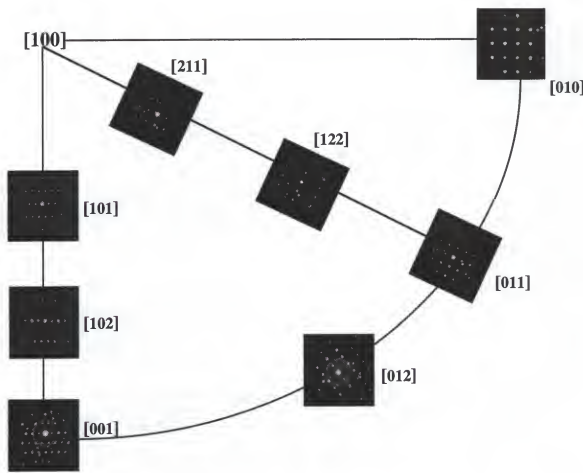
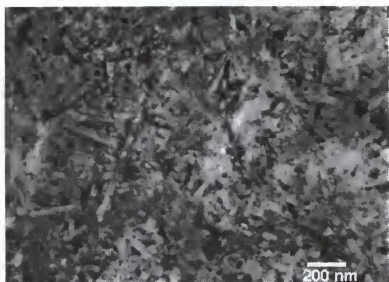
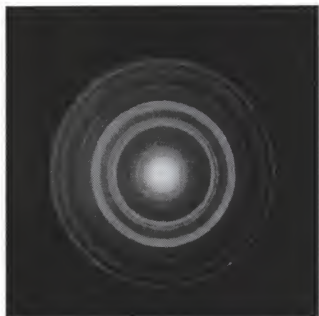


Figure 5.14. SAD patterns corresponding to several low index zones in m-HfBe crystallites, providing confirmation of Tanner's proposed Cmcm space group.



(a)



(b)

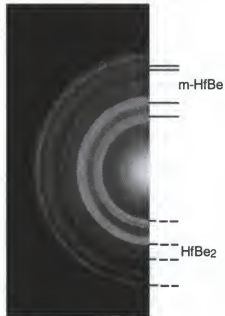
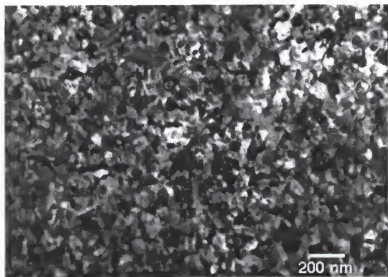
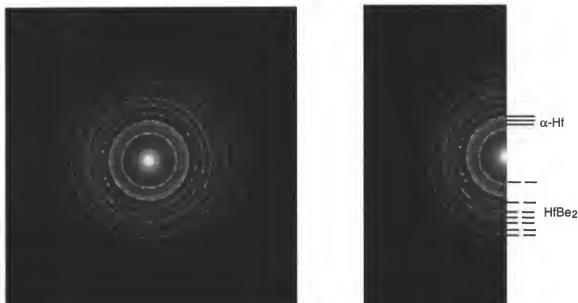


Figure 5.15. Hf-55Be annealed at 500°C for 12 minutes
(a) Bright Field (b) SAD Ring pattern.

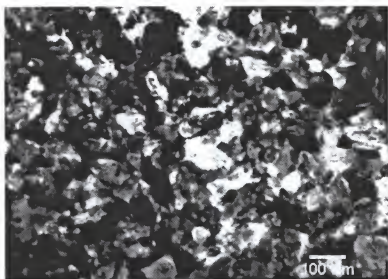


(a)

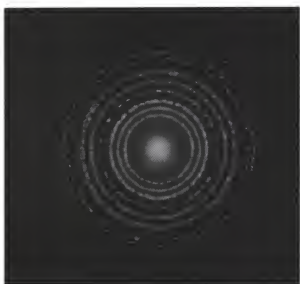


(b)

Figure 5.16. Hf-55Be sample annealed at 500°C for 15 min
(a) Bright Field (b) SAD ring pattern.



(a)



(b)



Figure 5.17. Hf-55Be sample annealed at 500°C for 30 min
(a) Bright Field (b) SAD ring pattern.

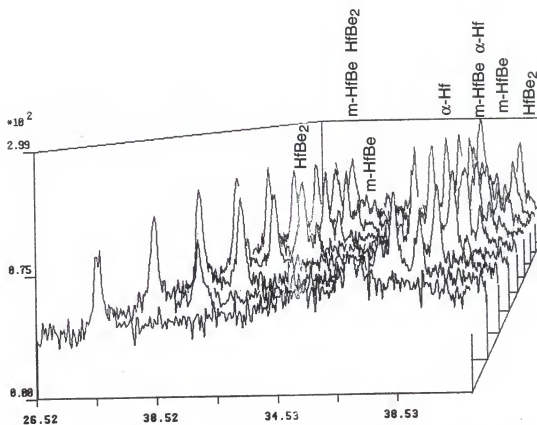


Figure 5.18. 3-D plot of High-temperature XRD data from an Hf-50Be sample continuously annealed to 650°C.

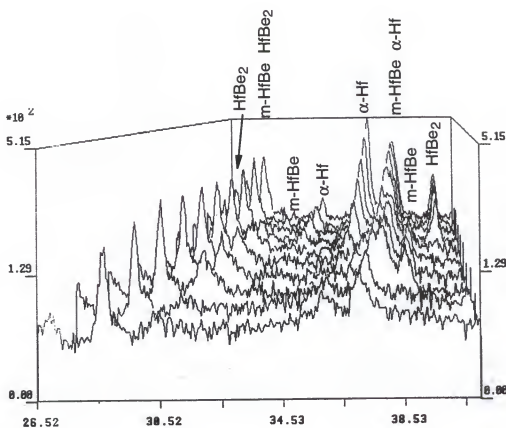
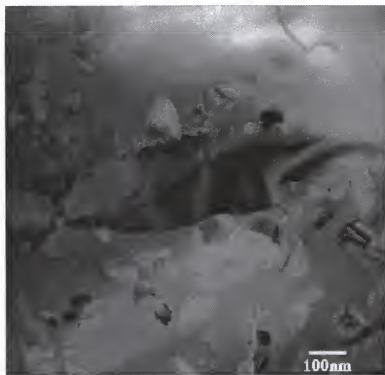
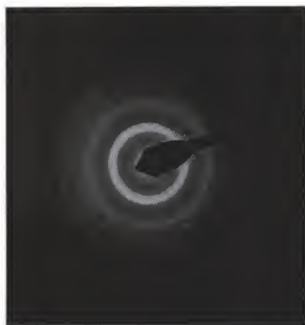


Figure 5.19. 3-D plot of High-temperature XRD data from an Hf-45Be sample continuously annealed to 650°C.



(a)



(b)

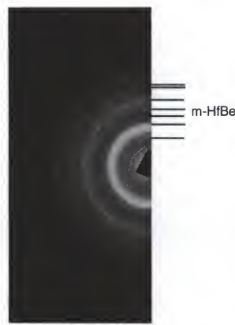


Figure 5.20. Hf-45Be in-situ annealed at approximately 515°C
(a) BFTEM of typical region and (b) SADP of same.

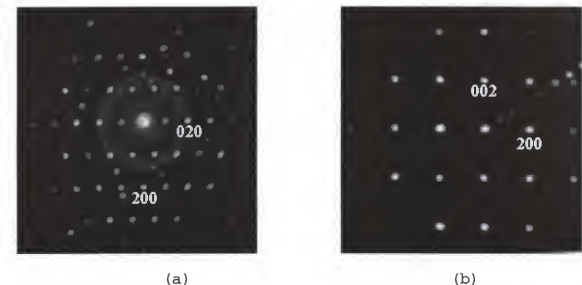


Figure 5.21. SAD patterns from primary m-HfBe phase
(a) $B=[001]$ and (b) $B=[010]$.

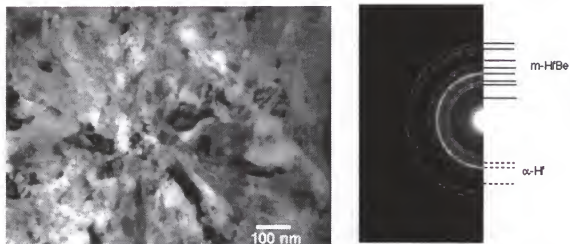
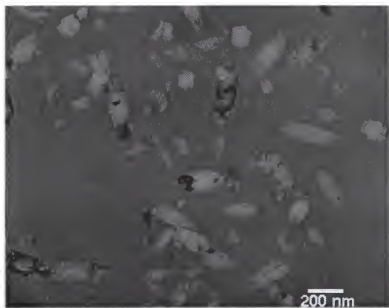
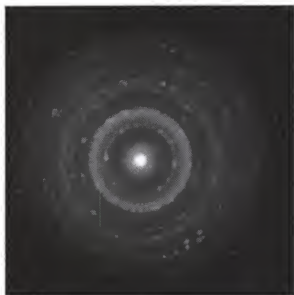


Figure 5.22. BFTEM and SADP of typical region of in-situ annealed Hf-45Be sample with primary and secondary phases.



(a)



(b)

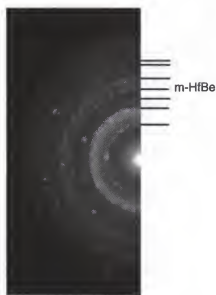
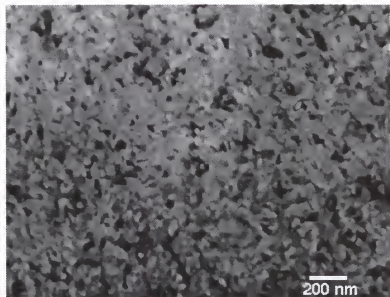


Figure 5.23. Hf-50Be in-situ annealed at approximately 515°C
(a) BF showing primary m-HfBe crystallites
(b) SAD ring pattern from crystallites.



(a)



(b)

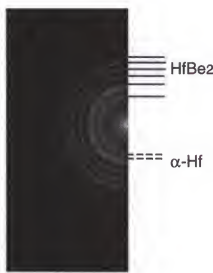
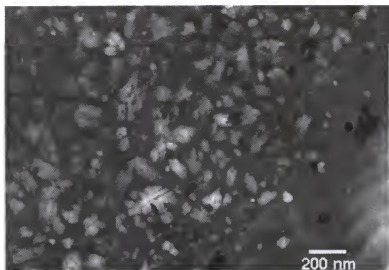
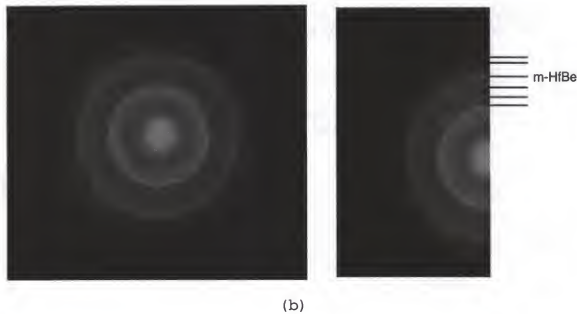


Figure 5.24. Hf-50Be in-situ annealed at approximately 515°C showing transformation of m-HfBe phase into the stable phases (a) with the corresponding SAD ring pattern (b).

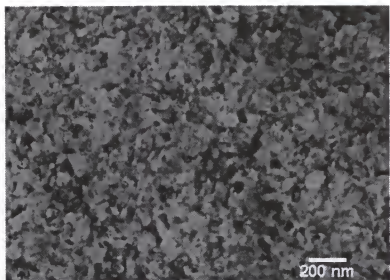


(a)

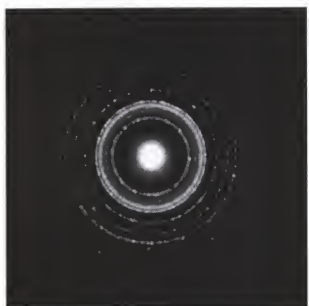


(b)

Figure 5.25. Hf-55Be in-situ annealed at approximately 525°C
(a) Primary m-HfBe crystallites in an amorphous matrix (b) SAD ring pattern from crystallites.



(a)



(b)

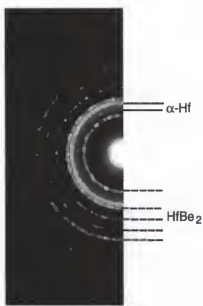
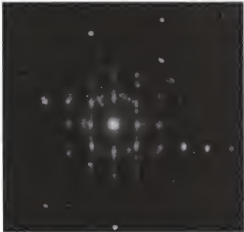


Figure 5.26. Hf-55Be in-situ annealed at approximately 515°C showing transformation of the m-HfBe phase into the stable phases (a) with the corresponding SAD ring pattern (b).



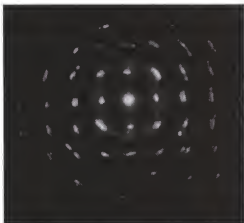
(a)



(b)

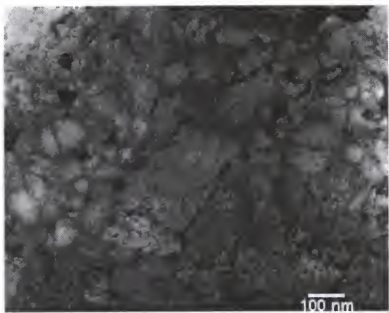


(c)

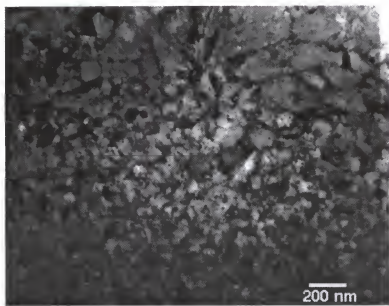


(d)

Figure 5.27. SADP's representing the decomposition of the m-HfBe phase displaying (a,b) streaking (c,d) spot broadening.



(a)



(b)

Figure 5.28. m-HfBe undergoing decomposition showing a "brush-stroke" appearance.

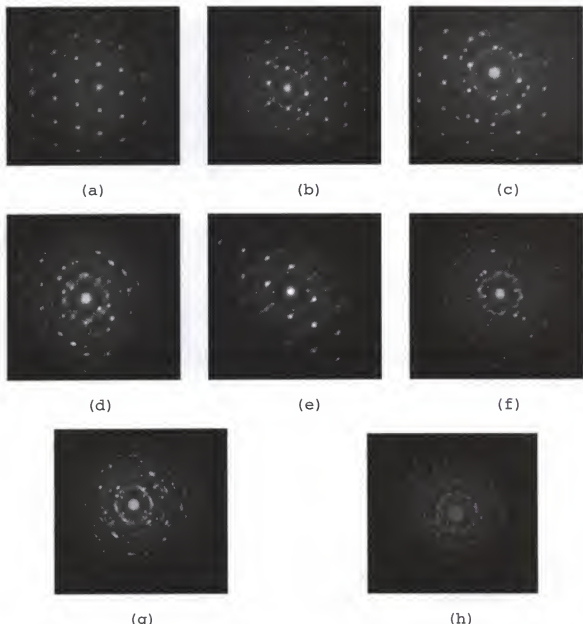


Figure 5.29. Transformation of an m-HfBe crystallite resulting in an SADP ring pattern corresponding to α -Hf + HfBe₂.

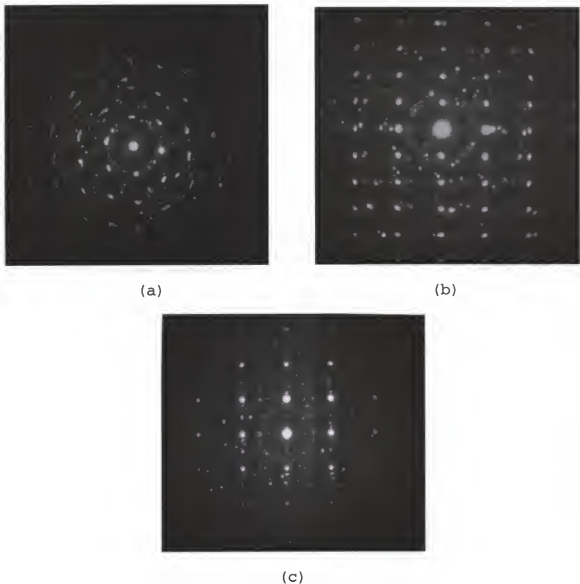


Figure 5.30. Transforming m-HfBe crystallites showing a lack of any orientation relationship between the crystallite (spot pattern) and the stable phases (rings).

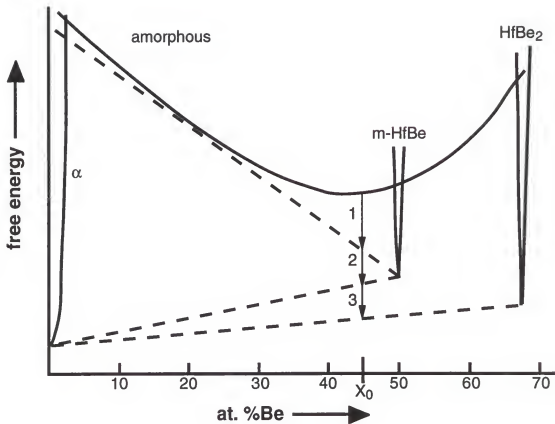


Figure 5.31. Schematic free energy curves showing the devitrification of an Hf-45Be alloy (1) primary, (2) metastable eutectoid, and (3) equilibrium eutectoid.

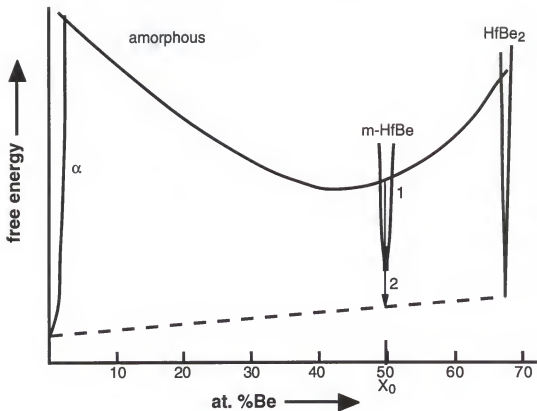


Figure 5.32. Schematic free energy curves showing the devitrification of an Hf-50Be alloy 91) polymorphic m-HfBe and (2) Equilibrium eutectoid.

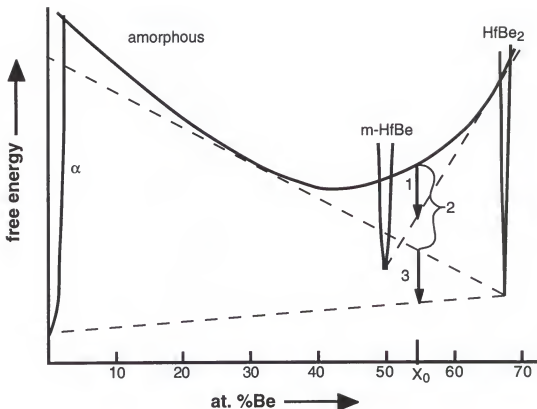


Figure 5.33. Schematic free energy curves depicting the possible "shut down" mechanism in a Hf-55Be alloy (1) primary m-HfBe, (2) primary $HfBe_2$, and (3) equilibrium eutectoid.

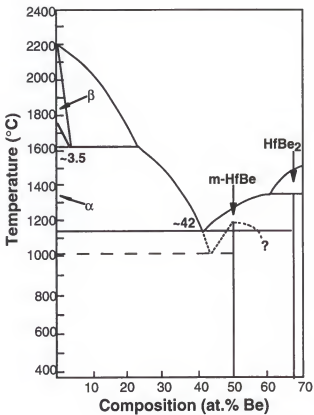


Figure 5.34. Metastable Hf-Be phase diagram as proposed from present research.

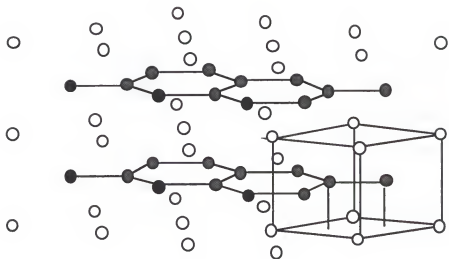


Figure 5.35. AlB_2 (hP3) crystal structure.

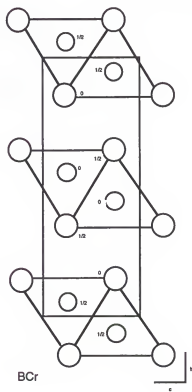


Figure 5.36. CrB (oC8) crystal structure.

CHAPTER 6
SUMMARY AND FUTURE WORK

6.1 Summary

A variety of processing and characterization techniques have been utilized to determine the relationship between metastable phases and stable faceting phases in faceted/non-faceted alloy systems. Characterization of both bulk and thin film microstructures has been performed in order to assure that any documented transformations were not sample size dependent. The conclusions of the present study are as follows:

1. Previous results for the behavior of Al-Ge alloys with 48-52 at% Ge have been confirmed and show that for faceting enriched compositions (52%Ge), no primary metastable phase was detected and overall no equilibrium between the monoclinic MOP and the stable faceting phase (β -Ge) was documented.

2 Amorphous thin film crystallization of an Al-55Ge film displayed eutectoid crystallization into the two stable phases during in-situ beam heating. For alloy system where formation of the amorphous phase is difficult-- very high

cooling rates needed-- rapid crystallization techniques are mandatory to even attempt to produce metastable phases and, as a result, the transformations occur very rapidly making characterization difficult.

3. Melt-spun Fe-B ribbons with 25 and 27 at% B respectively exhibit marked differences in their solidification microstructures. Specifically, the microstructure of melt-spun Fe-25B consisted of large cellular dendrites of metastable Fe_3B with interdendritic second phase whereas, the Fe-27B alloy was comprised of large cellular Fe_2B dendrites with an interdendritic second phase.

4 Evidence from the Fe-B study resulted in the development of a new metastable phase diagram consisting of a metastable eutectic between α -Fe and Fe_3B .

5. The behavior of alloys in the Fe-B system was consistent with that in the Al-Ge system with no documented equilibrium between the Fe_3B and Fe_2B phases.

6. While previous work on the Hf-Be system had suggested a eutectoid crystallization sequence for alloys with 45 at%Be, it is now clear that primary crystallization occurs initially indicating that XRD is not adequate to determine the transformation mechanisms clearly.

7. Amorphous Hf-Be ribbons of equiatomic composition displayed a polymorphic crystallization reaction to the m-HfBe phase. The m-HfBe phase was shown to be quite thermally stable resisting decomposition in bulk annealed ribbons for times up to 65 minutes at 500 C. This provides evidence that the m-HfBe phase may be only slightly metastable with respect to the two stable α -Hf and HfBe₂ phases.

8. The crystal structure of the m-HfBe phase was determined using CBED and conventional SAD and the space group was Cmcm consistent with the structure proposed by Tanner(29).

9. Ribbons with 55 at% Be developed primary m-HfBe crystallites upon heating but, at this composition, the m-HfBe decomposes rather quickly leaving a mixture of the two stable phases. A mechanism based on a sluggish/impaired growth phenomenon was proposed to explain the behavior in these alloys. Transformation of the m-HfBe was monitored and no orientation relationship was documented for the resulting stable phases thus indicating a displacive or eutectoid type transformation mode is not operative.

10. No evidence of equilibria between the metastable and stable faceting phases was observed in the three different faceted/non-faceted systems studied. This is consistent with the assertion that, in general, no

equilibrium will exist between the metastable phase and the stable faceting phase for faceted/non-faceted systems.

6.2 Future Work

1. One of the difficulties in doing studies based on the effects of composition or examining differences in microstructure processed under "similar" conditions is the slight variations in processing from sample to sample. In order to avoid this and hopefully make the work on the Hf-Be system more conclusive it would be beneficial to produce samples that would encompass a range of compositions in a sample with a small volume such that all of the various compositions could be processed simultaneously. For the Hf-Be system production of an amorphous thin film via a co-evaporation process onto a substrate (approximately 8mm diameter) should produce a film that is compositional modulation across the diameter of the substrate and then subsequently strips from the substrate could be annealed thus providing truly similar processing conditions for a wide range of compositions.

2. If possible identify a system where the metastable phase has a composition intermediate between two faceted phases.

3. Examination of the relationship between metastable disordered phases and stable faceting phase in faceted/non-faceted systems such as, Ag-Ge and Ag-Si.

LIST OF REFERENCES

1. B. C. Giessen, *Developments in the Structural Chemistry of Alloy Phases*, (Plenum, New York, 1979) 227-281.
2. R. W. Cahn, *Contemp. Phys.* **21**, 43 (1980).
3. P. Duwez, R. H. Willens, W. Klement, *J. Appl. Phys.* **31**, 1136 (1960).
4. R. W. K. Honeycomb, *Proceedings of 3rd Int. Conf. on Rapidly Quenched Metals* **1**, 73 (1978).
5. H. Jones, C. Suryanarayana, *J. Mater. Sci.* **8**, 705 (1973).
6. P. Ramachandrara, M. G. Scott, G. A. Chadwick, *Phil. Mg.* **25**, 961 (1972).
7. D. E. Polk, B. C. Giessen, *Metallic Glasses*, (ASM, Metals Park, 1978) 1-35.
8. W. Kurz, R. Trivedi, *Materials Science and Engineering* **a179/a180**, 46-51 (1994).
9. M. Lipschutz, Master's Thesis, University of Florida (1990).
10. W. J. Boettinger, J.H. Perepezko, *Proceedings of Symposium on Rapidly Solidified Crystalline Alloys*, Morristown, NJ (1985) pp.1-25.
11. D. Turnbull, *Metallurgical Transactions A* **12a**, 695-706 (1981).

12. U. Koster, *Acta Metall* **20**, 1361 (1972).
13. P. Predecki, B. C. Giessen, N. J. Grant, *Transactions of AIME* **233**, 1438 (1965).
14. C. Suryanarayana, T. R. Anantharaman, *Z. Metallkunde* **64**, 800 (1973).
15. B. Predel, G. Schluckebier, *Z. Metallkunde* **63**, 198 (1972).
16. M. G. Scott, *Z. Fur Metallkunde* **65**, 198 (1974)
17. M. Laridjani, K. D. Krishnanand, R. W. Cahn, *J. Mater. Sci* **11**, 1643 (1976).
18. M. Laridjani, R. W. Cahn, *Mater. Sci. Eng* **23**, 125 (1976).
19. P. Ramachandraraao, K. Lal, A. Singhdeo, K. Chattopadhyay, *Mater. Sci. Eng* **41**, 259 (1979).
20. M. J. Kaufman, H. L. Fraser, *Mater. Sci. Eng* **57**, L17 (1983).
21. M. J. Kaufman, H. L. Fraser, *Int. J. Rapid Solidification* **1**, 27 (1984-85).
22. M. J. Kaufman, H. L. Fraser, *Acta Metall* **33**, 191-203 (1985).
23. S. N. Ojha, K. Chattopadhyay, P. Ramachandraraao, *Mater. Sci. Eng* **73**, 177 (1985).
24. T. Laoui, *Dissertation at University of Washington* (1990).
25. T. Laoui, M. J. Kaufman, *Metallurgical Transactions A* **22a**, 2141-2151 (1991).

26. T. R. Anantharaman, P. Ramachandrara, C. Suryanarayana, S. Lele, K. Chattopadhyay, G.V.S. Sastri, and H.A. Davies, Eds., *Rapid Quenching of Aluminum Alloys* (1981).
27. M. J. Kaufman, J. E. Cunningham, H. L. Fraser, *Acta metall* **35**, 1181 (1987).
28. T. Laoui, M. J. Kaufman, *Scripta Metallurgica et Materialia* **30**, 1563-1567 (1994).
29. L. E. Tanner, *Acta Metallurgica* **28**, 1805-1816 (1980).
30. L. E. Tanner, *Scripta Metallurgica* **14**, 657-662 (1980).
31. U. Koster, U. Herold, in *Topics in Applied Physics* H. J. Guntherodt, H. Beck, Eds. (Springer-Verlag, Neuchatel, 1981).
32. J. L. Walter, S. Bartram, R. Russell, *Metallurgical Transactions A* **9A**, 803-814 (1978).
33. D. Oleszak, P. Glijer, H. Matyja, *Materials Science and Engineering* **a133**, 630-635 (1991).
34. Y. Khan, E. Kneller, M. Sostarich, *Z fur Metallkunde* **72** (1981).
35. O. T. Inal, C.V. Robino, L. Keller, *Journal of Materials Science* **16**, 3183-3192 (1981).
36. R. Ray, R. Hasegawa, *Solid State Communications* **27**, 471-474 (1978).
37. P. Duhaj, P. Svec, G. Vlasak, *Rapidly Quenched Metal* , 271-274 (1985).
38. M. Matsuura, *Solid State Communication* **30**, 231-233 (1979).
39. M. Gibson, G. Delamore, *Acta Metall.* **38**, 2621-2629 (1990).

40. R. Hasegawa, R. Ray, *J. Appl. Phys.* **49**, 4174-4179 (1978).
41. F. Luborsky, H. Lieberman, *Applied Physics Letters* **14**, 227 (1978).
42. R. T. Dehoff, *Thermodynamics in Materials Science*(McGraw-Hill, New York, 1994) pp 241-300.
43. M. Cohen, D. Turnbull, *J. Chem. Phys.* **52**, 3038 (1970).
44. M. Cohen, D. Turnbull, *J. Chem. Phys.* **31**, 1164 (1959).
45. D. E. Polk, B. C. Giessen, in *Metallic Glasses*. (1978) pp. 1-35.
46. F. Spapean, D. Turnbull,in Proc. 2nd Int. Conf. on Rapidly Quenched Metals N. Grant, B. Giessen Eds.,(MIT Press, Boston, 1976) 205.
47. P. Duwez, R. H. Willens, W. Klement, *Journal of Applied Physic* **5**, 992 (1960).
48. T. B. Massalski, C. G. Woychik, J. L. Murray, , R. Mehrabian, B. H. Kear, M. Cohen, Eds., Proc. 2nd Int. Conf. on Rapid Solidification Processing, Principles, and Technologies, Baton Rouge (Claitor's, 1980).
49. F. Spapean, R. Meyer, *Scripta Metall.* **10**, 257 (1976).
50. N. Marcus, D. Turnbull, *Materials Science and Engineering* **23**, 211-214 (1976).
51. I. W. Donald, H. A. Davies, *Journal of Non-Crystalline Solids* **30**, 77-85 (1978).
52. D. Turnbull, J. C. Fisher, *Journal of Chemical Physics* **17**, 71-73 (1949).
53. R. Becker, W. Doring, *Ann. d. Physik* **24**, 719 (1935).

54. K. Kelton, *Solid State Phys.* **45**, 75 (1991).
55. D. Turnbull, *Journal of Applied Physics* **21**, 1022-1028 (1950).
56. D. Turnbull, *Journal of Chemical Physics* **18**, 198-203 (1950).
57. H. Vogel, *Phys. A* **22**, 645 (1921).
58. G. S. Fulcher, *J. Am. Ceram. Soc.* **6**, 339 (1925).
59. A. L. Greer, *Journal of Non-crystalline Solids* **61-62**, 737 (1984).
60. D. Turnbull, *J. Chem. Phys.* **20**, 411 (1952).
61. G. Pound, V. LaMer, *J. Am. Ceram. Soc.* **74**, 2323 (1952).
62. A. Skapski, *Acta Metall.* **4**, 583 (1956).
63. F. Spapean, *Acta Metall.* **23**, 729 (1975).
64. R. Ewing, *Phil. Mag.* **25**, 778 (1972).
65. D. R. Uhlman, *J. Non-Cryst. Solids* **7**, 337 (1972).
66. J. Hoffman, *J. Chem. Phys.* **29**, 1192 (1958).
67. C. Thompson, F. Spapean, *Acta Metall.* **27**, 1855 (1979).
68. J. H. Perepezko, *Materials Science and Engineering a179/a180*, 52-56 (1994).
69. J. H. Perepezko, *Materials Science and Engineering a178*, 105-111 (1994).

70. A. L. Greer, *Metallurgical And Materials Transactions* **27a**, 549-555 (1996).
71. A. L. Greer, in *Summer School on Amorphous Metals* H. Matyja, P. Zielinski, Eds. (World Scientific Publishing Co, Singapore, 1985) pp. 68-112.
72. A. Greer, *Science* **267**, 1947-1951 (1995).
73. D. Uhlman, , *Materials Science Research* (Plenum, New York, 1969), vol. 4.
74. D. Turnbull, *J. Chem. Phys.* **64**, 609 (1962).
75. H. Rawson, *Inorganic Glass Forming System* (Academic Press, London, 1967).
76. M. Fine, *Phase Transformations in Condensed Systems* (MacMillan, New York, 1964).
77. P. Sarjeant, R. Roy, *Mater. Res. Bull.* **3**, 265 (1968).
78. J. Vreeswijk, R. Grossink, J. Stevels, *J. Non-Cryst. Solids* **16**, 15 (1974).
79. P. Shungu, R. Ozaki, *Metall. Trans. A* **7A**, 310 (1975).
80. H. Davies, B. Lewis, *Metall. Trans. A* **7A** (1976).
81. D. Turnbull, *Contemp. Phys.* **10**, 473 (1969).
82. W. Johnson, R. Mehl, *Trans. Metall. Soc. AIME* **135**, 416 (1939).
83. G. Cliff, G. Lorimer, *J. Micros.* **103**, 203 (1975).
84. J. Goldstein, D. Williams, G. Cliff, in *Principles of Analytical Electron Microscopy* D. Joy, A. Romig, J. Goldstein, Eds. (Plenum, New York, 1986) pp. 155.

85. H. S. Randhawa, *Phys. Stat. Sol* **37**, 313-320 (1976).
86. L. E. TANNER, R. RAY, *Acta Metallurgica* **27**, 1727-1747 (1979)
87. Y. Khan, *Z. fur Metallkunde* **73**, 624 (1982).
88. H. Das, *Metall. Trans.* **A14**, 953 (1983).
89. A. Sinha, B. Giessen, D. Polk, in *Treatise on Solid State Chemistry* N. Hannay, Ed. (Elsevier, London, 1981), vol. 3, pp. 1-81.
90. J. T. Taylor, *ACERS Bulletin* **74**, 81-83 (1995).
91. J. Spence, R. Carpenter, in *Principle of Analytical Electron Microscopy* D. Joy, A. Romig, J. Goldstein, Eds. (Plenum, New York, 1986) pp. 300.
92. T. Hanhn, Ed., *International Tables for Crystallography* (Kluwer Academic Publishers, Boston, 1989).
93. P. Boswell, G. Chadwick, *Scr. Metall.* **10**, 509 (1976).
94. H. Chen, L. Kimmerling, J. Poate, W. Brown, *Applied Phys. Lett* **32**, 361-463 (1978).
95. C. Chou, D. Turnbull, *J. Non-Cryst. Solids* **17**, 169 (1975).
96. R. Freed, J. Vandersonde, *Acta Metall.* **28**, 103-21 (1980).
97. D. Gupta, K. Tu, K. Asai, *Phys Rev Lett.* **35**, 796-99 (1975).
98. R. W. Cahn, *Contemporary Physics* **21**, 43 (1980).
99. U. Koster, U. Herold, H. Hillenbrand, H. Davis, *Journ. Mater. Sci* **15**, 2125-2128 (1980).

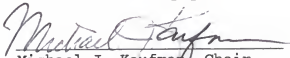
100. L. Kaufman, L. E. Tanner, *Calphad* **3**, 91-107 (1979).
101. N. Saunders, A. P. Miodownik, L. E. Tanner, *Rapidly Quenched Metals* , 191-195 (1985).
102. W. Pearson, *The Crystal Chemistry and Physics of Metals and Alloys* (Wiley--Interscience, New York, 1972).
103. M. Aziz, in *Undercooled Alloy Phases* E. Collings, C. Koch, Eds. (TMS, New Orleans, 1986) 375.

BIOGRAPHICAL SKETCH

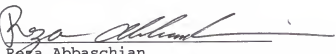
The author was born on October 15, 1969, in Jacksonville, Florida. He received his elementary education through both public and private schools in Jacksonville. In 1987, he graduated from The Bolles School. Immediately following his high school graduation, the author began attending the University of Tennessee. While at the University of Tennessee, the author pursued his Bachelor of Science degree in materials science and engineering. He graduated from the University of Tennessee in December of 1991. In January of 1992, the author enrolled at the University of Florida and began his Master of Science studies under the supervision of Dr. Richard Connell, Jr. In April of 1994, he received his M.S. degree and began his work toward his Ph.D. Since 1994, the author has worked for Dr. Michael Kaufman in the area of rapid solidification and phase transformations. In May of 1997, the author was awarded his Ph.D. and began work at Westinghouse--Savannah River Technology Center.

The author is married to the former Miss. Kimberly Suzanne Laxson and has one daughter, Laurel Elisabeth.

I certify that I have read this study and that in my opinion it conforms to acceptable standards of scholarly presentation and is fully adequate, in scope and quality, as a dissertation for the degree of Doctor of Philosophy.


Michael J. Kaufman, Chair
Professor of Materials
Science and Engineering

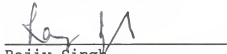
I certify that I have read this study and that in my opinion it conforms to acceptable standards of scholarly presentation and is fully adequate, in scope and quality, as a dissertation for the degree of Doctor of Philosophy.


Reza Abbaschian
Professor of Materials
Science and Engineering

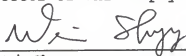
I certify that I have read this study and that in my opinion it conforms to acceptable standards of scholarly presentation and is fully adequate, in scope and quality, as a dissertation for the degree of Doctor of Philosophy.


Robert DeHoff
Professor of Materials
Science and Engineering

I certify that I have read this study and that in my opinion it conforms to acceptable standards of scholarly presentation and is fully adequate, in scope and quality, as a dissertation for the degree of Doctor of Philosophy.


Rajiv Singh
Associate Professor of
Materials Science and
Engineering

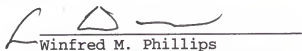
I certify that I have read this study and that in my opinion it conforms to acceptable standards of scholarly presentation and is fully adequate, in scope and quality, as a dissertation for the degree of Doctor of Philosophy.



Wei Shyy
Professor of Aerospace
Engineering, Mechanics
and Engineering Science

This dissertation was submitted to the Graduate Faculty of the College of Engineering and to the Graduate School and was accepted as partial fulfillment of the requirements for the degree of Doctor of Philosophy.

May, 1997


Winfred M. Phillips
Dean, College of Engineering

Karen A. Holbrook
Dean, Graduate School